PHYSICAL REVIEW D **75,** 064021 (2007)

Gravitational self-force on a particle in circular orbit around a Schwarzschild black hole

Leor Barack and Norichika Sago

School of Mathematics, University of Southampton, Southampton, SO17 1BJ, United Kingdom

(Received 15 January 2007; published 19 March 2007)

We calculate the gravitational self-force acting on a pointlike particle of mass μ, set in a circular geodesic orbit around a Schwarzschild black hole. Our calculation is done in the Lorenz gauge: For given orbital radius, we first solve directly for the Lorenz-gauge metric perturbation using numerical evolution in the time domain; we then compute the (finite) backreaction force from each of the multipole modes of the perturbation; finally, we apply the ''mode-sum'' method to obtain the total, physical self-force. The *temporal* component of the self-force (which is gauge invariant) describes the dissipation of orbital energy through gravitational radiation. Our results for this component are consistent, to within the computational accuracy, with the total flux of gravitational-wave energy radiated to infinity and through the event horizon. The *radial* component of the self-force (which is gauge dependent) is calculated here for the first time. It describes a conservative shift in the orbital parameters away from their geodesic values. We thus obtain the $O(\mu)$ correction to the specific energy and angular momentum parameters (in the Lorenz gauge), as well as the $O(\mu)$ shift in the orbital frequency (which is gauge invariant).

DOI: 10.1103/PhysRevD.75.064021 PACS numbers: 04.25.Nx, 04.30.Db, 04.70.Bw

I. INTRODUCTION AND SUMMARY

The problem of calculating the backreaction force, or *self-force* (SF), experienced by a point particle as it moves in curved spacetime is now understood well enough to allow actual computations of this effect in systems comprising of a small object orbiting a large black hole. The fundamental formulation of the problem and its solution was set in works by DeWitt and Brehme [1] (electromagnetic SF), Mino, Sasaki, and Tanaka [2] and Quinn and Wald [3] (gravitational SF), and Quinn [4] (scalar field SF). An alternative formulation was introduced by Detweiler and Whiting [5], also clarifying the relation between the SF picture (''forced motion on a background geometry'') and the standard description based on the principle of equivalence (''geodesic motion in a perturbed geometry''). A number of authors later devised a practical calculation method for the SF in black hole spacetimes—the ''mode-sum scheme''—which is based on multipole decomposition of the retarded field, and relies on standard methods of black hole perturbation theory [6–10]. This method has since been implemented by various authors on a case-by-case basis, so far mostly for calculations of the scalar field SF. Work so far included the cases of a static particle in Schwarzschild [11] or along the rotation axis of a Kerr black hole [12]; radial plunge trajectories [13] and circular orbits around a Schwarzschild black hole [14–17]; and ongoing work on eccentric orbits in Schwarzschild [18,19]. The *gravitational* SF has been calculated so far only for radial trajectories in Schwarzschild [20] and for static (nongeodesic) particles in Schwarzschild [21]. The case of an orbiting particle has been tackled only under the post-Newtonian (PN) approximation [22]. A comprehensive review of the subject, including a self-contained account of SF fundamentals, is provided by Poisson [23]. For a snapshot of the current activity in the field, the reader may refer to [24].

One of the main motivations for the work on self-forces draws from the need to devise accurate theoretical waveforms for the gravitational radiation from extreme mass-ratio inspirals (EMRIs)—of the prime targets for LISA, the planned space-based gravitational wave detector [25]. This requires solving the SF problem in the gravitational case, for generic inspiral orbits around a Kerr black hole. The main challenge in extending the analysis from the scalar-field toy model to the gravitational case has to do with the gauge freedom in the latter case. The problem can be summarized as follows. The gravitational perturbation in the vicinity of the point particle is best described using the *Lorenz* gauge (see Appendix A), which preserves the local isotropic nature of the point singularity. On the other hand, the field equations that govern the global evolution of the metric perturbation are more tractable in gauges which comply well with the global symmetry of the black hole background—best known examples of which are the ''radiation'' gauges [26] or the Regge-Wheeler gauge [27]. Now, in calculating the local SF we need, essentially, to subtract a suitable local, divergent piece of the perturbation from the full (retarded) perturbation field. In doing so, both fields (local and global) must be given in the same gauge; the ''gauge problem'' arises since the two fields are normally calculated in different gauges. Indeed, the only fully worked-out example of the gravitational SF so far is the case of radial orbits in Schwarzschild [20], where the gauge problem is avoided simply because, in this particular setup, the singular piece of the Regge-Wheeler perturbation happens to coincide with that of the Lorenz-gauge perturbation.

One approach to the problem has been to try and calculate the local divergent piece in one of the ''global'' gauges—specifically the Regge-Wheeler gauge in the Schwarzschild spacetime [28–30]. This has been implemented so far only within a post-Newtonian approximation

[22]. In the current work we take a complementary approach: We solve the perturbation equations, and obtain the global retarded field, directly in the Lorenz gauge. The calculation is therefore done entirely within the Lorenz gauge, the ''subtraction'' procedure necessary for constructing the SF is implemented in a straightforward way, and the gauge problem is avoided altogether. Other advantages of working in the Lorenz gauge include the fact that the field equations then take a fully hyperbolic form (making them especially suitable for time-domain integration); and the fact that the Lorenz-gauge metric perturbation is better behaved near the particle compared with the perturbation in other gauges [31] (which, again, makes it more suitable for numerical implementation). The better regularity of the Lorenz-gauge perturbation is manifested in the behavior of individual multipole modes of the field [32]: It is well known, for example, that the multipole modes of the Regge-Wheeler perturbation from a point particle in Schwarzschild generally show a discontinuity across the particle. In contrast, the modes of the Lorenz-gauge perturbation are always continuous at the particle.

Our ''all-Lorenz-gauge'' approach is made possible (at least is the Schwarzschild case) following a recent work by Barack and Lousto [33] (hereafter BL), which provided a practical formulation of the Lorenz-gauge perturbation equations in the Schwarzschild geometry. Our calculation is based on the BL formulation, and our numerical code incorporates the code developed in BL (with a few improvements). In the current work we focus on circular geodesic orbits, for simplicity. However, since our treatment is based on a time-domain evolution, our code could be amended to deal with generic orbits (in Schwarzschild) in an almost straightforward manner. We shall discuss this extension of the analysis in the concluding section, and also comment there on the important extension to the Kerr case.

Our calculation of the SF proceeds as follows. We first write down the 10 (coupled) evolution equations for the 10 tensorial-harmonic components of the Lorenz-gauge metric perturbation, in the form given in BL (with a slight modification). The energy-momentum of the orbiting particle is represented by a suitable delta-function distribution, whose tensor-harmonic components serve as sources for the evolution equations. For given orbital radius and given multipole numbers l and m we solve the equations numerically through time-domain evolution in $1+1$ dimensions (time + radius), using a 2nd-order convergent finite-difference scheme on a staggered grid based on characteristic coordinates. We integrate long enough to allow any spurious initial radiation to dissipate efficiently (this takes ~ 3 orbital periods for strong-field orbits). We then record the values of the metric perturbation and its temporal and radial derivatives at the location of the particle. [Recall that individual multipole modes of the perturbation are continuous at the particle. Their first derivatives have a finite jump discontinuity across the particle (in the radial direction) and so we record both values of the derivatives.] We repeat this calculation for all multipole modes with $2 \leq l \leq l_{\max}$, where $l_{\max}$ is determined experimentally so that our standard of accuracy (of $<10^{-3}$ fractional error in the final SF) is met. In practice we found it sufficient to take $l_{\max} = 15$ for the radial component and $l_{\max} = 5$–9 for the t component (depending on the orbital radius). The modes $l = 0, 1$ are calculated separately, using the method of Detweiler and Poisson [34]. The values of the metric perturbation and its derivatives at the particle are then used as input for the mode-sum scheme. Within this scheme, each of the modes is ''regularized'' using functions known analytically [8–10], and the sum over modes yields the desired SF.

Our main results are summarized in Tables IV and V (along with Fig. 8). The tables display the values of both radial and temporal components of the SF as a function of the orbital radius. The temporal component of the SF is simply related, in our stationary circular-orbit setup, to the rate of change of the orbital energy parameter, and hence to the flux of energy carried in gravitational waves to null infinity and down the event horizon. Our results demonstrate this energy balance, which provides a reassuring validity test for our code. The radial component of the SF (which is itself gauge dependent) describes the conservative backreaction effect on the orbital parameters. Based on our results we calculate the conservative shift in the energy and angular momentum of the circular geodesic, as well as the shift in the orbital frequency—the latter being gauge invariant. Our results for the shifts are plotted in Figs. 9 and 10.

To check the validity and robustness of our code, and assess the accuracy of our results, we performed the following tests. (i) *Numerical convergence*: For each of the modes calculated, we repeated our computation with a handful of different numerical resolutions, checking that the answer converges quadratically to a limiting value with decreasing step size. To determine the limiting value we used a Richardson extrapolation (over step size), and recorded the estimated error from this extrapolation. (ii) *Effect of spurious initial waves*: We compared the values of the SF at two different (late) evolution times (recall that in our stationary setup the physical SF does not depend on time), in order to assess the effect of residual spurious waves. (iii) *Large l behavior*: The behavior of the SF modes at large multipole numbers l is known analytically with high precision [see Eqs. (20)–(22) below]. We verified that our numerically calculated modes have the right behavior at large l, through all three known leading terms in the $1/l$ expansion. This agreement is necessary, in fact, for a successful implementation of the mode-sum scheme. (iv) *Error from large-l tail*: The mode-sum scheme involves summation over all modes l. In practice we computed all modes up to $l = l_{\max}$, and used an ex-

trapolation to estimate the contribution from the remaining $l > l_{\max}$ tail. We assessed and recorded the error from this extrapolation. (v) *Comparison of one-sided forces*: The mode-sum scheme can be implemented in two essentially independent ways, by using either the "external" or the "internal" values of the SF modes (i.e., values calculated by taking one-sided derivatives of the metric perturbation from outside or inside the orbit, respectively). Of course, the final value of the SF should not depend on our choice. We used our code to work out both values, and checked that they are the same to a very good accuracy. We recorded the (tiny) difference between the two values. Our total computation error was taken to be the combined error from the extrapolation over step size [item (i) above], the deviation from stationarity [item (ii) above], the extrapolation over l [item (iv)], and the small discrepancy between external and internal values. We made sure that this combined error is kept under 0.1%. (vi) *Comparison with energy flux*: We checked that the computed temporal component of the SF balances the flux of energy to null infinity and down the horizon. We found an excellent agreement.

The structure of this paper is as follows. In Sec. II we review the formalism for constructing the metric perturbation in the Lorenz gauge and for calculating the SF via the mode-sum scheme (focusing on the case of circular orbits in Schwarzschild). We also discuss the effect of the SF on the geodesic parameters (energy, angular momentum, angular velocity), and how these depend on the choice of gauge. Section III describes our numerical method, including a detailed description of the finite-difference scheme. In Sec. IV we present a few validation tests for our code, and explain how we estimated the computation error. Section V gives the results: We tabulate both temporal and radial components of the SF as a function of the orbital radius, and calculate the shift in the orbital parameters due to the conservative piece of the force. Finally, in Sec. VI we discuss the extension of this work to more general orbits in Schwarzschild, and to orbits in Kerr.

Throughout this work we use standard geometrized units (with $c = G = 1$) and metric signature $(-+++)$. The Riemann tensor is defined as in Ref. [35].

II. REVIEW OF THEORY: SELF-FORCE IN LORENZ GAUGE

A. Orbital setup and equation of motion

Consider a pointlike particle of mass μ, in a circular orbit around a Schwarzschild black hole with mass $M \gg \mu$. Let the worldline of the particle be represented by $x^\alpha = x^\alpha_{\rm p}(\tau)$, with tangent four-velocity $u^\alpha = dx^\alpha_{\rm p}/d\tau$. At the limit $\mu \to 0$ (i.e., neglecting SF effects) the particle traces a geodesic $x^\alpha_{\rm p} = x^\alpha_0(\tau)$, with associated four-velocity $u^\alpha_0 = dx^\alpha_0/d\tau$. Without limiting the generality, we adopt a Schwarzschild coordinate system t, r, θ, φ in which the orbit is confined to the equatorial plane. Then

$$x^\alpha_0(\tau) = [t_0(\tau), r_0 = \text{const}, \theta_0 = \pi/2, \varphi_0(\tau)]. \quad (1)$$

This circular geodesic can be parametrized by the radius r_0, or, alternatively, by the angular velocity (with respect to time t)

$$\Omega_0 \equiv d\varphi_0/dt = \sqrt{M/r_0^3}, \quad (2)$$

by the specific energy parameter

$$\mathcal{E}_0 \equiv -u_{0t} = (1 - 2M/r_0)(1 - 3M/r_0)^{-1/2}, \quad (3)$$

or by the specific angular momentum parameter

$$\mathcal{L}_0 \equiv u_{0\varphi} = (Mr_0)^{1/2}(1 - 3M/r_0)^{-1/2}. \quad (4)$$

The subscripts "0" here indicate that the above are values associated with the geodesic x^α_0 (below we will consider the correction to these values due the SF effect). As always in our perturbative treatment, tensorial indices are "raised" and "lowered" using the background metric.

Now assume that μ is finite (but still very small compared to M). The equation of motion can be written as

$$\mu \frac{D^2 x^\alpha_{\rm p}}{D\tau^2} = \mu \frac{Du^\alpha}{D\tau} = F^\alpha, \quad (5)$$

where the covariant derivatives are taken with respect to the *background* (Schwarzschild) geometry, and $F^\alpha[\sim O(\mu^2)]$ is the gravitational SF. Clearly, the symmetry of the problem implies $F^\theta = 0$. Also, assuming the four-velocity is kept normalized along the worldline, i.e., $u_\alpha u^\alpha = -1$, we have $D(u_\alpha u^\alpha)/D\tau = 0$, leading to $u_\alpha F^\alpha = 0$, and the four components of the SF are not independent. In the circular-orbit case we have the relation $u_t F^t + u_\varphi F^\varphi = 0$, which we may write, through leading order in μ, as

$$F^\varphi = (\mathcal{E}_0/\mathcal{L}_0)F^t. \quad (6)$$

Hence, we need only calculate two of the components of the SF: the r component and (say) the t component. For simplicity we shall refer to these as the "radial" and "temporal" components. Our goal would be to calculate both components, as a function of the orbital radius r_0. Note that it is sufficient, for the sake of obtaining the leading-order $[O(\mu^2)]$ SF, to assume that the motion is momentarily geodesic.

The SF affects the motion of the particle in two ways: First, $-u_t$ and u_φ are no longer conserved over time, so we can speak of the "rate of change" of the energy and angular momentum of the orbit. Second, at each given time, the values of $-u_t$ and u_φ are shifted with respect to their corresponding geodesic values $-u_{0t}$ and $u_{0\varphi}$. In the case of a circular orbit, the first, "dissipative" effect is due entirely to F^t (and F^φ), while the second, "conservative" effect is due entirely to F^r. To see this, start by defining $\mathcal{E} \equiv -u_t$ and $\mathcal{L} \equiv u_\varphi$. The t and φ components of Eq. (5) immediately give

$$\frac{d\mathcal{E}}{d\tau} = -\mu^{-1}F_t \quad \text{and} \quad \frac{d\mathcal{L}}{d\tau} = \mu^{-1}F_\varphi, \tag{7}$$

respectively, describing the dissipative effect of the SF. The change of energy and angular momentum is precisely balanced by the flux of energy and angular momentum carried away by gravitational waves. For the conservative effect, consider the r component of Eq. (5), along with the normalization condition $u_\alpha u^\alpha = -1$. Solving these two equations simultaneously for u^t and u^φ (recalling $u^r = du^r/d\tau = 0$), one obtains $(u^t)^2 = r_0(1 - r_0F_r/\mu)/(r_0 - 3M)$ and $(u^\varphi)^2 = (M/r_0^2 - F^r/\mu)/(r_0 - 3M)$, or, through $O(\mu)$,

$$\mathcal{E} = \mathcal{E}_0\left[1 - \left(\frac{r_0}{2\mu}\right)F_r\right], \qquad \mathcal{L} = \mathcal{L}_0\left[1 - \left(\frac{r_0^2}{2M\mu}\right)F^r\right]. \tag{8}$$

Given the radial component of the SF, the last two equations give the conservative shift in the energy and angular momentum parameters. It is also useful to look at the shift in the orbital frequency $\Omega \equiv d\varphi_p/dt = u^\varphi/u^t$. Based on the above expressions for u^t and u^φ we obtain, through $O(\mu)$,

$$\Omega = \Omega_0\left[1 - \left(\frac{r_0(r_0 - 3M)}{2M\mu}\right)F_r\right], \tag{9}$$

which describes the shift in the "frequency at infinity" due to the conservative piece of the SF.

B. Gauge dependence

It is important to understand how the above quantities depend on the choice of gauge. Let $h_{\alpha\beta}[\sim O(\mu)]$ be the metric perturbation due to the particle, given in a specific gauge. Consider an infinitesimal gauge transformation

$$x^\mu \to x'^\mu = x^\mu + \xi^\mu. \tag{10}$$

This will change the metric perturbation by an amount

$$\delta_\xi h_{\alpha\beta} \equiv h'_{\alpha\beta} - h_{\alpha\beta} = -(\xi_{\alpha;\beta} + \xi_{\beta;\alpha}). \tag{11}$$

It will also induce a change in the SF, given by [31]

$$\begin{aligned}\delta_\xi F_\alpha &\equiv F'_\alpha - F_\alpha \\ &= \mu\left[[g_{\alpha\lambda}(x_0) + u_{0\alpha}u_{0\lambda}]\frac{D^2\xi^\lambda}{D\tau^2}\right. \\ &\quad \left. + R_{\alpha\mu\lambda\nu}(x_0)u_0^\mu\xi^\lambda u_0^\nu\right].\end{aligned} \tag{12}$$

Here $g_{\alpha\lambda}(x_0)$ and $R_{\alpha\mu\lambda\nu}(x_0)$ are the background (Schwarzschild) metric and Riemann tensors, respectively, evaluated at the particle.

We now assume that the original gauge is "physically reasonable." In our case (a circular equatorial orbit in Schwarzschild), this would mean that the perturbation $h_{\alpha\beta}$ in that gauge reflects the stationarity of the problem, and also retains the symmetry of reflection through the equatorial plane. The Lorenz gauge (see Appendix A for definition) is an example of such a gauge. Restricting our discussion to gauge transformations within the family of "physically reasonable" gauges, we should clearly require, in our case, $d\xi_\alpha/d\tau = 0$, as well as $\xi^\theta = 0$. From Eq. (12) we then get $\delta_\xi F_t = \delta_\xi F_\theta = \delta_\xi F_\varphi = 0$, along with

$$\delta_\xi F_r = -3\mu(\mathcal{L}_0^2/r_0^4)\xi^r. \tag{13}$$

Hence, "physically reasonable" gauge transformations may affect the radial component of the SF (they do so if they have $\xi^r \neq 0$), but not the other components.

One immediate consequence of the above is that the quantities $d\mathcal{E}/d\tau$ and $d\mathcal{L}/d\tau$ in Eq. (7) are invariant under a gauge transformation (as should be expected on physical grounds). However, the quantities $\mathcal{E}$ and $\mathcal{L}$ themselves are *not* gauge invariant. To see this, use Eq. (13) in Eq. (8), along with $\mathcal{E}_0 \to \mathcal{E}_0 + (d\mathcal{E}_0/dr_0)\xi^r$, and $\mathcal{L}_0 \to \mathcal{L}_0 + (d\mathcal{L}_0/dr_0)\xi^r$. [Note here that the coordinate location r_0 (and hence also $\mathcal{E}_0$ and $\mathcal{L}_0$) is obviously *not* gauge invariant: Under the gauge transformation (10) we have simply $r_0 \to r_0 + \xi^r$.] Denoting $\delta_\xi\mathcal{E} \equiv \mathcal{E}' - \mathcal{E}$ and $\delta_\xi\mathcal{L} \equiv \mathcal{L}' - \mathcal{L}$, and keeping only terms linear in ξ^r, one then obtains the following gauge transformation formulas for $\mathcal{E}$ and $\mathcal{L}$:

$$\delta_\xi\mathcal{E} = \frac{2M/r_0^2}{\sqrt{1 - 3M/r_0}}\xi^r, \qquad \delta_\xi\mathcal{L} = \frac{2}{\sqrt{1 - 3M/r_0}}\xi^r. \tag{14}$$

We can construct orbital parameters that *are* invariant under the transformation (10). One example is the frequency Ω, given in Eq. (9). Detweiler pointed out recently [36] that the combination $\mathcal{E} - \Omega\mathcal{L} \equiv S$ is also gauge invariant (for circular orbits). For both Ω and S, it is a straightforward exercise to show that, under the gauge transformation (10),

$$\delta_\xi\Omega = 0, \qquad \delta_\xi S = \delta_\xi(\mathcal{E} - \Omega\mathcal{L}) = 0. \tag{15}$$

C. Metric perturbation in Lorenz gauge

In this work we calculate the SF in the Lorenz gauge. This will require knowledge of the full (retarded) metric perturbation $h_{\alpha\beta}$ in the Lorenz gauge. We briefly review here the construction of the Lorenz-gauge perturbation, referring the reader to BL [33] for further details.

In the formulation by BL, the Lorenz-gauge metric perturbation in Schwarzschild is constructed through [37]

$$h_{\alpha\beta} = \frac{\mu}{2r}\sum_{l=0}^{\infty}\sum_{m=-l}^{l} h_{\alpha\beta}^{lm}, \tag{16}$$

with

$$h^{lm}_{tt} = (\bar{h}^{(1)} + f\bar{h}^{(6)})Y^{lm}, \qquad h^{lm}_{tr} = f^{-1}\bar{h}^{(2)}Y^{lm}, \qquad h^{lm}_{rr} = f^{-2}(\bar{h}^{(1)} - f\bar{h}^{(6)})Y^{lm}, \qquad h^{lm}_{t\theta} = r(\bar{h}^{(4)}Y^{lm}_{\mathrm{V1}} + \bar{h}^{(8)}Y^{lm}_{\mathrm{V2}}),$$
$$h^{lm}_{t\varphi} = r\sin\theta(\bar{h}^{(4)}Y^{lm}_{\mathrm{V2}} - \bar{h}^{(8)}Y^{lm}_{\mathrm{V1}}), \qquad h^{lm}_{r\theta} = rf^{-1}(\bar{h}^{(5)}Y^{lm}_{\mathrm{V1}} + \bar{h}^{(9)}Y^{lm}_{\mathrm{V2}}), \qquad h^{lm}_{r\varphi} = rf^{-1}\sin\theta(\bar{h}^{(5)}Y^{lm}_{\mathrm{V2}} - \bar{h}^{(9)}Y^{lm}_{\mathrm{V1}}),$$
$$h^{lm}_{\theta\theta} = r^2(\bar{h}^{(3)}Y^{lm} + \bar{h}^{(7)}Y^{lm}_{\mathrm{T1}} + \bar{h}^{(10)}Y^{lm}_{\mathrm{T2}}), \qquad h^{lm}_{\theta\varphi} = r^2\sin\theta(\bar{h}^{(7)}Y^{lm}_{\mathrm{T2}} - \bar{h}^{(10)}Y^{lm}_{\mathrm{T1}}),$$
$$h^{lm}_{\varphi\varphi} = r^2\sin^2\theta(\bar{h}^{(3)}Y^{lm} - \bar{h}^{(7)}Y^{lm}_{\mathrm{T1}} - \bar{h}^{(10)}Y^{lm}_{\mathrm{T2}}). \tag{17}$$

Here $f = 1 - 2M/r$, and Y^{lm}_{V1}, Y^{lm}_{V2}, Y^{lm}_{T1}, and Y^{lm}_{T2} are angular functions constructed from the standard spherical harmonics $Y^{lm}(\theta, \varphi)$ through

$$Y^{lm}_{\mathrm{V1}} \equiv \frac{1}{l(l+1)}Y^{lm}_{,\theta} \quad (\text{for } l > 0),$$
$$Y^{lm}_{\mathrm{V2}} \equiv \frac{1}{l(l+1)}\sin^{-1}\theta Y^{lm}_{,\varphi} \quad (\text{for } l > 0),$$
$$Y^{lm}_{\mathrm{T1}} \equiv \frac{(l-2)!}{(l+2)!}[\sin\theta(\sin^{-1}\theta Y^{lm}_{,\theta})_{,\theta} - \sin^{-2}\theta Y^{lm}_{,\varphi\varphi}] \quad (\text{for } l > 1), \tag{18}$$
$$Y^{lm}_{\mathrm{T2}} \equiv \frac{2(l-2)!}{(l+2)!}(\sin^{-1}\theta Y^{lm}_{,\varphi})_{,\theta} \quad (\text{for } l > 1).$$

The functions $\bar{h}^{(i)lm}$ [$i = 1, \ldots, 10$; the indices l, m were omitted in Eq. (17) for brevity] depend on r and t only, and form our basic set of perturbation fields. These time-radial fields are obtained as solutions to the coupled set of hyperbolic [in a 2-dimensional (2D) sense], scalarlike equations

$$\Box\bar{h}^{(i)lm} + \mathcal{M}^{(i)l}_{(j)}\bar{h}^{(j)lm} = S^{(i)lm} \quad (i = 1, \ldots, 10). \tag{19}$$

Here "$\Box$" represents the 2D scalar-field operator, $\Box = \partial_{uv} + V(r)$, where v and u are the standard Eddington-Finkelstein null coordinates, and the potential is $V(r) = \frac{1}{4}f[2M/r^3 + l(l+1)/r^2]$. The "coupling" terms $\mathcal{M}^{(i)l}_{(j)}\bar{h}^{(j)lm}$ involve first derivatives of the $\bar{h}^{(j)lm}$'s at most (no second derivatives), and $S^{(i)lm}$ are source terms. Both $\mathcal{M}^{(i)l}_{(j)}\bar{h}^{(j)lm}$ and $S^{(i)lm}$ are given explicitly in Appendix A for our circular-orbit case. In addition to the evolution equations (19), the functions $\bar{h}^{(i)lm}$ also satisfy four elliptic equations, which stem from the gauge conditions. These "constraint" equations are also given in Appendix A. The set (19) incorporates "divergence dissipating" terms, which guarantee that violations of the Lorenz-gauge conditions are efficiently damped during the evolution [33].

BL demonstrated in [33] how Eqs. (19) can be evolved numerically (for $l \geq 2$), in the time domain, with a delta-function source term representing an orbiting point particle. They also demonstrated that the solutions preserve the Lorenz-gauge condition throughout the late-time evolution (initial violations of the gauge conditions are suppressed over a time scale $\sim M$).

The perturbation modes $l = 0$ and $l = 1$ require a separate treatment. For $l = 0$, the set (19) reduces to 4 equations (for $\bar{h}^{(1,2,3,6)}$), which describe the spherically symmetric, monopole mass perturbation. Section III D of BL gives the solution for the Lorenz-gauge monopole perturbation in analytic form (based on analysis by Detweiler and Poisson [34]). For $l = 1$, $m = \pm 1$, the set (19) reduces to 6 equations (for $\bar{h}^{(1-6)}$). These describe the rotational dipole piece of the perturbation, which is (in Newtonian terms) due to the motion of the black hole about the center of mass of the black hole-particle system. The Lorenz-gauge solution for this mode was obtained by Detweiler and Poisson [34], using a procedure that reduces the problem to the solution of 3 coupled ordinary differential equations (see also Ori [38] for a fully analytic weak-field treatment). Finally, for $l = 1$, $m = 0$—the axisymmetric dipole perturbation—the set (19) reduces to a single equation (for $\bar{h}^{(8)}$), describing the perturbation in the angular momentum due to the particle. The analytic solution for this mode was obtained long ago by Zerilli [39], and identified in [34] as a Lorenz-gauge solution. BL later obtained analytic Lorenz-gauge solutions for *all* axisymmetric ($m = 0$) modes with odd l. These are given in Sec. III C of BL.

In what follows we will prescribe the construction of the gravitational SF directly in terms of the functions $\bar{h}^{(i)lm}$.

D. Self-force via the mode-sum method

In the mode-sum scheme, the gravitational SF is calculated through [7–10]

$$F^{\alpha} = \sum_{l=0}^{\infty}[[F^{\alpha l}_{\mathrm{full}}(x_0)]_{\pm} - A^{\alpha}_{\pm}L - B^{\alpha}], \tag{20}$$

where $L \equiv l + 1/2$, and $F^{\alpha l}_{\mathrm{full}}$ are the modes of the "full" force, obtained from the modes of the full (retarded) metric perturbation in a manner described below. The subscript $\pm$ refers to the two possible values of $F^{\alpha l}_{\mathrm{full}}$ at x_0, resulting from taking one-sided radial derivatives of the metric perturbation from either $r \to r_0^+$ or $r \to r_0^-$ (recall that the modes of the Lorenz-gauge metric perturbation are continuous, but their gradients generally have a finite jump discontinuity across the particle). $A^{\alpha}_{\pm}$ and B^{α} are the "regularization parameters," which are known analytically. For circular equatorial geodesics in Schwarzschild we have $A^{\alpha}_{\pm} = B^{\alpha} = 0$ for $\alpha = t, \theta, \varphi$, and

$$A^{r}_{\pm} = \mp\frac{\mu^2}{r_0^2}\left(1 - \frac{3M}{r_0}\right), \tag{21}$$

$$B^{r} = \frac{\mu^2\mathcal{E}_0^2}{\pi(\mathcal{L}_0^2 + r_0^2)^{3/2}}[\hat{E}(w) - 2\hat{K}(w)], \tag{22}$$

where $\hat{K}(w) \equiv \int_0^{\pi/2}(1 - w\sin^2 x)^{-1/2}dx$ and $\hat{E}(w) \equiv \int_0^{\pi/2}(1 - w\sin^2 x)^{1/2}dx$ are complete elliptic integrals of

the first and second kind, respectively, and $w \equiv (r_0/M - 2)^{-1}$. The final SF F^α can be calculated using either external $(+)$ or internal $(-)$ values; the difference $[F^{\alpha l}_{\rm full}(x_0)]_\pm - A^\alpha_\pm L$ is guaranteed to be direction independent. One can also use the average value, $\bar{F}^{\alpha l}_{\rm full} \equiv \{[F^{\alpha l}_{\rm full}]_+ + [F^{\alpha l}_{\rm full}]_-\}/2$, in terms of which the mode-sum formula takes the more compact form

$$F^\alpha = \sum_{l=0}^{\infty} [\bar{F}^{\alpha l}_{\rm full}(x_0) - B^\alpha]. \tag{23}$$

Recall here we are interested in the r and t components of the SF. For the r component, the contribution from the individual full modes is $\propto L$ at large L, and the sum over $[F^{\alpha l}_{\rm full}(x_0)]_\pm$ diverges. However, the contribution from the regularized modes $[F^{rl}_{\rm full}(x_0)]_\pm - A^r_\pm L - B^r$ falls off as $\propto L^{-2}$ at large L, and their sum converges (and gives the correct physical SF). The regularized modes admit the large-l expansion

$$F^{rl}_{\rm reg} \equiv [F^{rl}_{\rm full}(x_0)]_\pm - A^r_\pm L - B^r = \frac{D_2}{L^2} + \frac{D_4}{L^4} + \cdots, \tag{24}$$

where $D_2, D_4, \ldots$ are coefficients that may depend on the orbital parameters, but not on L. As for the t component: In the special case of a circular orbit the temporal full-force modes require no regularization (recall $A^t = B^t = 0$), and their sum converges. In fact, in this case the mode sum can be shown to converge exponentially at large l (this will be demonstrated experimentally in Sec. IV below). For later convenience we write

$$F^{tl}_{\rm reg} \equiv F^{tl}_{\rm full}, \tag{25}$$

and the mode-sum formula becomes, for either the r or the t component,

$$F^\alpha = \sum_{l=0}^{\infty} F^{\alpha l}_{\rm reg}. \tag{26}$$

E. Construction of the full-force modes

We now describe the construction of the full modes $[F^{\alpha l}_{\rm full}(x_0)]_\pm$ out of the Lorenz-gauge perturbation fields $\bar{h}^{(i)lm}$.

First, following [7], define the "full-force field" as a tensor field at arbitrary spacetime point x, for a given (fixed) worldline point x_0 (where the SF is to be calculated):

$$F^\alpha_{\rm full}(x; x_0) = \mu k^{\alpha\beta\gamma\delta} \bar{h}_{\beta\gamma;\delta}. \tag{27}$$

Here $\bar{h}_{\alpha\beta} = h_{\alpha\beta} - \frac{1}{2} g_{\alpha\beta} g^{\mu\nu} h_{\mu\nu}$ is the "trace-reversed" Lorenz-gauge metric perturbation at x, and

$$k^{\alpha\beta\gamma\delta}(x; x_0) = g^{\alpha\delta} u^\beta u^\gamma/2 - g^{\alpha\beta} u^\gamma u^\delta - u^\alpha u^\beta u^\gamma u^\delta/2 + u^\alpha g^{\beta\gamma} u^\delta/4 + g^{\alpha\delta} g^{\beta\gamma}/4, \tag{28}$$

where $g^{\alpha\delta}$ is the background metric at x, and u^α are the values of the contravariant components of the four-velocity at x_0 (treated as fixed coefficients). Obviously, the full force $F^\alpha_{\rm full}$ diverges for $x \to x_0$ (like $\sim$distance^{-2}).

Next, expand the metric perturbation in tensor harmonics as in Eq. (16), and substitute in Eq. (27). Taking the limits $r \to r_0$ and $t \to t_0$ (but maintaining the θ, φ dependence), the full force takes the form

$$\begin{aligned}[F^\alpha_{\rm full}(\theta, \varphi; r_0, t_0)]_\pm = \frac{\mu^2}{r_0^2} \sum_{l=0}^{\infty} \sum_{m=-l}^{l} \{ & f^{\alpha lm}_{0\pm} Y^{lm} \\ & + f^{\alpha lm}_{1\pm} \sin^2\theta Y^{lm} + f^{\alpha lm}_{2\pm} \cos\theta \sin\theta Y^{lm}_{,\theta} \\ & + f^{\alpha lm}_{3\pm} \sin^2\theta Y^{lm}_{,\theta\theta} \\ & + f^{\alpha}_{4\pm} (\cos\theta Y^{lm} - \sin\theta Y^{lm}_{,\theta}) \\ & + f^{\alpha lm}_{5\pm} \sin\theta Y^{lm}_{,\theta} + f^{\alpha lm}_{6\pm} \sin^3\theta Y^{lm}_{,\theta} \\ & + f^{\alpha lm}_{7\pm} \cos\theta \sin^2\theta Y^{lm}_{,\theta\theta} \}, \end{aligned} \tag{29}$$

where $Y^{lm}(\theta, \varphi)$ are the spherical harmonics, and the coefficients $f^{\alpha lm}_{n\pm}$ are constructed from the perturbation fields $\bar{h}^{(i)lm}$ and their first r and t derivatives, all evaluated at x_0. The labels $+/-$ correspond to taking external/internal r derivatives, respectively. The explicit expressions for the $f^{\alpha lm}_{n\pm}$'s are quite lengthy, and we give them separately, in Appendix B.

The individual l modes in Eq. (29) are *not* quite yet the full-force modes needed in the mode-sum formula (20): A little complication arises because the mode-sum formula requires the decomposition of the full force in *scalar* harmonics. That is, to obtain the modes $[F^{\alpha l}_{\rm full}(x_0)]_\pm$ for use in Eq. (20) we are required to ignore the vectorial nature of the full force, and expand each of its components in *scalar* harmonics. To obtain this, we need only reexpand all angular functions in Eq. (29) in spherical harmonics, and rearrange the terms in the sum. The necessary expansion formulas are given in Appendix C. We find that each of the tensor-harmonic l modes in Eq. (29) couples to a finite number of scalar harmonics (there is no coupling between different m modes). For the r component, each tensor-harmonic l generally couples to 5 scalar-harmonic modes l' with $l - 2 \le l' \le l + 2$; for the t component, it generally couples to the 7 modes $l - 3 \le l' \le l + 3$. It should be commented that this finite coupling is characteristic of *all* (equatorial) orbits in Schwarzschild, not necessarily circular (although in general both t and r components would involve coupling to 7 scalar harmonics). We also comment that, in our circular-orbit case, it is not quite necessary to expand the t component in scalar harmonics, since this component requires no regularization and so the mode sum can be evaluated directly using the tensor-harmonic expansion. In this work we nevertheless choose to expand the t component too in spherical harmonics, for two reasons: First, this would allow us to test our general treatment of the coupling between modes, since the computed value of the t component of the SF could readily be verified by comparing with the flux of radiated energy. Second, our code could then be more easily adapted to deal with eccentric orbits, where scalar-

harmonic decomposition of both r and t components is necessary.

Hence, we now reexpand Eq. (29) in spherical harmonics (using the relations given in Appendix C), then rearrange the terms in the sum by collecting all terms with the same scalar-harmonic multipole number l, and, finally, set $\theta \to \theta_0$ and $\varphi \to \varphi_0$. The resulting "scalar harmonic" l modes of the full force take the final form

$$[F^{\alpha l}_{\rm full}(x_0)]_\pm = \frac{\mu^2}{r_0^2}\sum_{m=-l}^{l} Y^{lm}(\theta_0,\varphi_0)\times\{\mathcal{F}^{\alpha l-3,m}_{(-3)} + \mathcal{F}^{\alpha l-2,m}_{(-2)} + \mathcal{F}^{\alpha l-1,m}_{(-1)} + \mathcal{F}^{\alpha lm}_{(0)} + \mathcal{F}^{\alpha l+1,m}_{(+1)} + \mathcal{F}^{\alpha l+2,m}_{(+2)} + \mathcal{F}^{\alpha l+3,m}_{(+3)}\}_\pm, \tag{30}$$

where

$$\begin{aligned}
\mathcal{F}^{\alpha lm}_{(-3)} &= \zeta^{lm}_{(+3)} f^{\alpha lm}_{6\pm} + \xi^{lm}_{(+3)} f^{\alpha lm}_{7\pm},\\
\mathcal{F}^{\alpha lm}_{(-2)} &= \alpha^{lm}_{(+2)} f^{\alpha lm}_{1\pm} + \beta^{lm}_{(+2)} f^{\alpha lm}_{2\pm} + \gamma^{lm}_{(+2)} f^{\alpha lm}_{3\pm},\\
\mathcal{F}^{\alpha lm}_{(-1)} &= \epsilon^{lm}_{(+1)} f^{\alpha lm}_{4\pm} + \delta^{lm}_{(+1)} f^{\alpha lm}_{5\pm} + \zeta^{lm}_{(+1)} f^{\alpha lm}_{6\pm} + \xi^{lm}_{(+1)} f^{\alpha lm}_{7\pm},\\
\mathcal{F}^{\alpha lm}_{(0)} &= f^{\alpha lm}_{0\pm} + \alpha^{\alpha lm}_{(0)} f^{\alpha lm}_{1\pm} + \beta^{lm}_{(0)} f^{\alpha lm}_{2\pm} + \gamma^{lm}_{(0)} f^{\alpha lm}_{3\pm},\\
\mathcal{F}^{\alpha lm}_{(+1)} &= \epsilon^{lm}_{(-1)} f^{\alpha lm}_{4\pm} + \delta^{lm}_{(-1)} f^{\alpha lm}_{5\pm} + \zeta^{lm}_{(-1)} f^{\alpha lm}_{6\pm} + \xi^{lm}_{(-1)} f^{\alpha lm}_{7\pm},\\
\mathcal{F}^{\alpha lm}_{(+2)} &= \alpha^{lm}_{(-2)} f^{\alpha lm}_{1\pm} + \beta^{lm}_{(-2)} f^{\alpha lm}_{2\pm} + \gamma^{lm}_{(-2)} f^{\alpha lm}_{3\pm},\\
\mathcal{F}^{\alpha lm}_{(+3)} &= \zeta^{lm}_{(-3)} f^{\alpha lm}_{6\pm} + \xi^{lm}_{(-3)} f^{\alpha lm}_{7\pm},
\end{aligned} \tag{31}$$

with the various coefficients α, β, γ, δ, ϵ, ζ, and ξ given in Appendix C. Note $f^r_{6\pm} = f^r_{7\pm} = 0$, so that Eq. (30) simplifies considerably for the r component. The spherical harmonic $Y^{lm}(\theta_0,\varphi_0)$ is given explicitly, for $\theta_0 = \pi/2$, by

$$Y^{lm}(\pi/2,\varphi_0) = e^{im\varphi_0}\times\begin{cases}(-1)^{(l+m)/2}\left[\frac{(2l+1)(l+m-1)!!(l-m-1)!!}{4\pi(l+m)!!(l-m)!!}\right]^{1/2}, & l-m \text{ even}\\ 0, & l-m \text{ odd.}\end{cases} \tag{32}$$

Hence, for given l, only m modes with even $l-m$ contribute to the sum in Eq. (30). A further simplification arises since the individual m modes in the sum in Eq. (30) are invariant under $m \to -m$, which allows us to fold the $m<0$ part of the sum over to $m>0$. In practice, therefore, one is required to compute only $l/2+1$ m-modes for each even l-mode, and $(l+1)/2$ m-modes for each odd l-mode. Finally, note $\alpha^{lm}_{(+2)} = \beta^{lm}_{(+2)} = \gamma^{lm}_{(+2)} = \epsilon^{lm}_{(+1)} = \delta^{lm}_{(+1)} = \zeta^{lm}_{(+1)} = \xi^{lm}_{(+1)} = \zeta^{lm}_{(+3)} = \xi^{lm}_{(+3)} = 0$ for $l<0$, such that no functions $f^{\alpha lm}_n$ with $l<0$ occur in Eq. (30).

F. Summary of prescription for constructing the Lorenz-gauge SF

Start by calculating the Lorenz-gauge perturbation fields $\bar{h}^{(i)lm}$ (10 of which for each $l\geq 2$, m), by solving (numerically) the field equations (19). Obtain the modes $l=0,1$ of $\bar{h}^{(i)lm}$ through the procedure described at the end of Sec. II C. Construct the functions f^r_n and f^t_n using the formulas in Appendix B, and then construct the quantities $\mathcal{F}$ through Eqs. (31). Use these in Eq. (30) to obtain the scalar-harmonic l-modes of the full force, $[F^{\alpha l}_{\rm full}(x_0)]_\pm$. Incorporate the full-force modes in the mode-sum formula (20) [or (23)] to obtain the SF.

III. NUMERICAL IMPLEMENTATION

In this section we summarize the numerical method used to calculate the SF through the mode-sum formula (20). The evolution of the Lorenz-gauge field equations (19) was described in BL, but we will briefly review this method here—mainly in order to supplement a few details of the finite-difference scheme left out in BL. We then describe the numerical construction of the regularized SF modes, and the technique used to evaluate the infinite sum over l. There are three main sources of numerical error in our calculation: (i) error from the finite-grid discretization (which, in the procedure described below, comes from the error in a Richardson-type extrapolation to zero grid size); (ii) error from estimation of the large-l tail of the mode-sum series; and (iii) error from residual spurious waves resulting from the imperfection of initial data. We explain how all these errors are monitored and controlled in our calculation.

A. Metric perturbation: finite-difference scheme for $l \geq 2$

To solve Eqs. (19) for the various modes $l\geq 2$ we use characteristic time-domain evolution on a fixed 2D staggered double-null grid based on v, u coordinates. The numerical domain is depicted in Fig. 2 of BL. The evolution starts with characteristic initial data on two initial "rays" $v=v_0$ and $u=u_0$, taken such that the vortex v_0, u_0 corresponds to $r=r_0$ with initial time $t_0=0$. The circular-orbit worldline then traces a straight vertical line through the grid, connecting the "lower" and "upper" vertices (see Fig. 2 of BL). In this setup the worldline cuts through grid points. This does not cause a problem, since the Lorenz-gauge perturbation modes are continuous at the worldline. For initial data we simply take $\bar{h}^{(i)lm}=0$ along $v=v_0$ and $u=u_0$, for all i. This sparks a burst of spurious radiation at the initial vortex, which, however, dies off efficiently over time and leaves very little trace after 1–2 orbital periods of evolution (we demonstrate this below).

Our finite-difference scheme (particularly the handling of the delta-function source term) is based on the method first introduced by Lousto and Price [40] and later imple-

mented by a number of authors [13,20,41,42]. In this method, the finite-difference equation is obtained by approximating the (2D) *integral* of both sides of the field equation over a grid cell, at a suitable accuracy. This automatically deals with the delta-function singularity on the right-hand side of the equation. For the following discussion, consider Fig. 1: Suppose that we have already solved for all $\bar{h}^{(i)lm}$'s at the grid points numbered 2, 3, and 4. Denote the values calculated at these points by $\bar{h}^{(i)}_2$, $\bar{h}^{(i)}_3$, and $\bar{h}^{(i)}_4$, respectively, (we omit here the indices l, m for brevity), and let the sides of the grid cell be $\Delta v = \Delta u = h$. We are interested in obtaining $\bar{h}^{(i)}_1$, the value of the $\bar{h}^{(i)}$'s at point 1.

Consider first the principal part of the field equations (19). For any of the ten i's, it reads $\bar{h}^{(i)}_{,uv}$. This term is integrated exactly over the grid cell, to give

$$\iint_{\text{cell}} \bar{h}^{(i)}_{,uv} du dv = \bar{h}^{(i)}_1 - \bar{h}^{(i)}_2 - \bar{h}^{(i)}_3 + \bar{h}^{(i)}_4. \tag{33}$$

Since the $\bar{h}^{(i)}$'s are continuous at the worldline, the above integral holds even for grid cells crossed by the particle. The remaining part of the left-hand side of the field equations (19) includes three types of terms, of the form $V_1(r)\bar{h}^{(i)}$, $V_2(r)\bar{h}^{(i)}_{,r}$, and $V_3(r)\bar{h}^{(i)}_{,v}$, where the $V(r)$'s are known radial functions. As for terms of the first two types, we can approximate their integrals over the grid cell as

$$\iint_{\text{cell}} V_1(r)\bar{h}^{(i)} du dv = \frac{1}{2} h^2 V_1(r_c)(\bar{h}^{(i)}_2 + \bar{h}^{(i)}_3) + \begin{cases} O(h^3) & \text{(particle)}, \\ O(h^4) & \text{(no particle)}, \end{cases} \tag{34}$$

$$\iint_{\text{cell}} V_2(r)\bar{h}^{(i)}_{,r} du dv = h f^{-1}(r_c) V_2(r_c)(\bar{h}^{(i)}_3 - \bar{h}^{(i)}_2) + \begin{cases} O(h^3) & \text{(particle)}, \\ O(h^4) & \text{(no particle)}, \end{cases} \tag{35}$$

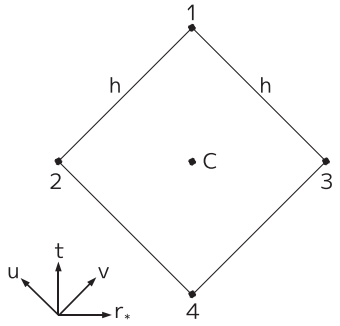

FIG. 1. A numerical grid cell, of dimensions $h \times h$ (see description in the text). Our 2D grid is based on characteristic (Eddington-Finkelstein) coordinates v and u. These are related to the Schwarzschild coordinates through $v = t + r_*$ and $u = t - r_*$, where $r_* = r + 2M \ln[r/(2M) - 1]$.

where r_c is the value of r at point C in the middle of the cell (see Fig. 1). The case indicated as "particle" refers to grid cells crossed by the worldline. "No particle" refers to grid cells not crossed by the worldline. The difference in the error terms arises because the $\bar{h}^{(i)}$'s generally have discontinued r derivatives across the worldline. We can accommodate a local error term of $O(h^3)$ along the worldline, as the worldline is crossed only once in each evolution time step, and so such an error accumulates over time to give a global error of only $O(h^2)$.

Terms of the form $V_3(r)\bar{h}^{(i)}_{,v}$ require a more careful treatment. For these we will need information from outside the grid cell of Fig. 1. Consider Fig. 2, showing an extended area around the central point C, now including also points 5–9. We assume all functions $\bar{h}^{(i)}_2$-$\bar{h}^{(i)}_9$ have been calculated before, and we need to obtain $\bar{h}^{(i)}_1$. The figure shows two special cases: In "case A" the worldline crosses the point C; in "case B" it crosses "just to the right" of point C, through points 3 and 6. The integral over the term $V_3(r)\bar{h}^{(i)}_{,v}$ can be approximated, in the various cases, through

$$\iint_{\text{cell}} V_3(r)\bar{h}^{(i)}_{,v} du dv = \frac{1}{2} h V_3(r_c) \times \begin{cases} 2\bar{h}^{(i)}_3 - \bar{h}^{(i)}_4 - \frac{1}{2}\bar{h}^{(i)}_5 - \frac{1}{2}\bar{h}^{(i)}_6 + O(h^3) & \text{(Case A)}, \\ \bar{h}^{(i)}_3 - \bar{h}^{(i)}_2 + 3\bar{h}^{(i)}_4 - 2\bar{h}^{(i)}_6 - 2\bar{h}^{(i)}_8 + \bar{h}^{(i)}_9 + O(h^3) & \text{(Case B)}, \\ 3\bar{h}^{(i)}_3 - 3\bar{h}^{(i)}_4 - \bar{h}^{(i)}_5 + \bar{h}^{(i)}_6 + O(h^4) & \text{(no particle)}, \end{cases} \tag{36}$$

where "no particle" refers to the most common case, in which the particle passes through neither point C nor point 3. There are, of course, alternative schemes which approximate this integral at the same order of accuracy. We have chosen the particular scheme in (36) as we found it experimentally stable.

Finally, we need to integrate the source term $S^{(i)lm}$ on the right-hand side of the field equations [the explicit form of the source term is given in Eq. (A11) of Appendix A]. Thanks to the delta function in $S^{(i)}$ we can work out the integral over the grid cell exactly. We find

$$\iint_{\text{cell}} S^{(i)lm} du dv = 8\pi \mathcal{E}_0 \alpha^{(i)} f^{-1}(r_c) \times h \times \text{sinc}(m\Omega_0 h/2) e^{-im\Omega_0 t_c} \times \begin{cases} Y^{lm*}(\pi/2, 0), & \text{for } i = 1\text{–}7, \\ Y^*_{,\theta}(\pi/2, 0), & \text{for } i = 8\text{–}10, \end{cases} \tag{37}$$

where t_c is the value of t at point C, an asterisk denotes complex conjugation, the coefficients $\alpha^{(i)}$ are those given in Eqs. (A12), and $\text{sinc}(x) \equiv (\sin x)/x$ for any $x \neq 0$, with $\text{sinc}(0) = 1$.

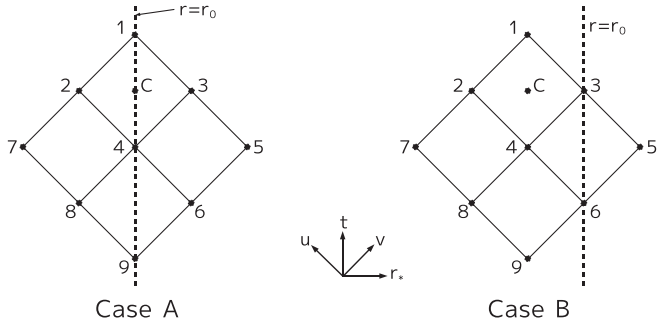

FIG. 2. Finite-difference scheme for terms in the field equations involving single v derivatives (diagrams to go with the description in the text). The dashed line represents the worldline, with two cases shown.

Integrating the field equations (19) using the above Eqs. (33)–(37), we can solve for the $\bar{h}^{(i)}$'s at point 1 given the values calculated in previous steps of the evolution. In this scheme we have to keep two $v = \text{const}$ data vectors at each (advanced) time step. The local finite-differentiating error at each grid point scales as $\sim h^4$, except for points belonging to Cases A or B (Fig. 2), for which the local error scales as $\sim h^3$. Since the total number of steps scales as $\sim h^{-2}$, and the number of steps belonging to Cases A or B scales as h^{-1}, we expect the error accumulated over the entire evolution to scale as $\sim h^2$.

B. Metric perturbation: Monopole and dipole modes

The monopole and dipole modes are dealt with separately. For $l = 0$ we use the analytic solution for the $\bar{h}^{(i)}$'s from Sec. III D of BL. For the mode $l = 1$, $m = 0$ we use the analytic solution from Sec. III C therein. For the mode $l = m = 1$ we follow the method of Detweiler and Poisson [34], which involves solving (numerically) a coupled set of 3 ordinary differential equations, with boundary conditions at infinity and along the horizon, and with matching conditions across the particle.

One may attempt to compute the modes $l = 0$, 1 also using the evolution Eqs. (19) (which reduce to four equations for $l = 0$, six equations for $l = m = 1$, and one equation for $l = 1$, $m = 0$). In practice, however, the system (19), in its present form, does not seem to evolve stably for these modes: For $l < 2$, some of the potential functions in these equations turn negative for some r values outside the black hole, apparently rendering the evolution unstable. This is not a serious problem in our present analysis, as we simply derive these two modes using other methods. The problem will have to be address when extending the analysis to noncircular orbits, for which analytic (or semianalytic) solutions are not yet at hand. One may then either attempt to derive analytic (or semianalytic) $l = 0$, 1 solutions for eccentric orbits; or, alternatively, attempt to find a reformulation of the evolution equations suitable for $l = 0$, 1.

C. Taking derivatives of the metric perturbation

The construction formulas for the r and t components of the SF require the derivatives $\bar{h}^{(i)}_{,r}$ and $\bar{h}^{(i)}_{,t}$, both evaluated at the particle. For the t derivatives we can simply make the substitution $\partial_t \to -im\Omega_0$, since in the circular-orbit case the fields $\bar{h}^{(i)}$ are stationary and depend upon t only through $[e^{im\varphi_0(t)}]^* \propto e^{-im\Omega_0 t}$. The r derivatives are taken numerically, using the finite-difference formula

$$\bar{h}^{(i)}_{,r}|_{\pm} = \mp \frac{3\bar{h}^{(i)}_0 - 4\bar{h}^{(i)}_{\pm 1} + \bar{h}^{(i)}_{\pm 2}}{2hf(r_0)} + O(h^2), \qquad (38)$$

where the various quantities refer to the diagram in Fig. 3: $\bar{h}^{(i)}_0$ is the value calculated on the worldline, at a given time, and $\bar{h}_{\pm 1}$ and $\bar{h}_{\pm 2}$ are the values at points ± 1 and ± 2, respectively. Recall $f(r_0) = 1 - 2M/r_0$. The subscripts $+/-$ refer to one-sided derivatives taken from r_0^+ or r_0^-. This scheme allows for discontinued r derivatives, which we expect some of the $\bar{h}^{(i)}$'s to have. The scheme gives the local derivative with an error that scales as $\sim h^2$—the same as the accumulated error in the $\bar{h}^{(i)}$. Hence, we expect the total finite-differentiation error in the SF to scale as $\sim h^2$.

Once we have at hand the various $\bar{h}^{(i)}$'s and their derivatives at the particle, we can construct the various scalar-harmonic modes of the full force, $[F^{tl}_{\text{full}}(x_0)]_{\pm}$ and $[F^{rl}_{\text{full}}(x_0)]_{\pm}$, using Eq. (30). [Recall that to obtain a single scalar-harmonic mode of the full force we need to calculate all tensor-harmonic modes of the perturbation with multipole numbers between $l - 2$ and $l + 2$ ($l - 3$ to $l + 3$ for the t component).] We then construct the regularized modes $F^{\alpha l}_{\text{reg}}$ through Eqs. (24) and (25). We use this procedure to calculate all modes up to $l = 15$ for the radial component, and up to $l = 4$–9 (depending on r_0) for the temporal component. (For the two radii $r_0 = 6M$ and $r_0 = 100M$ we obtain all modes of the radial component up to $l = 25$; we use the extra mode information in testing the validity of our numerical procedure—see below.)

Of course, the stationarity of our problem allows us to choose any point along the orbit for calculating the force. We need to make sure, though, that this point is taken late enough in the evolution, where the effect of initial spurious

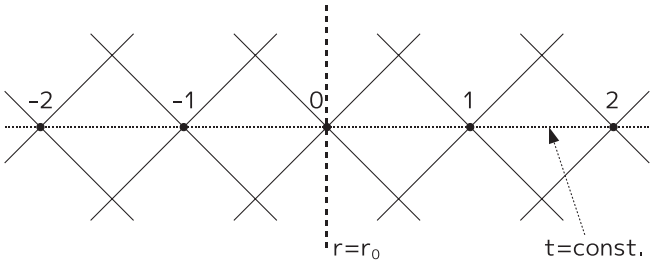

FIG. 3. Diagram to explain how r derivatives are taken at the worldline (see description in the text). The dashed line represents the particle's trajectory on the numerical grid. The SF is calculated at the point labeled "0."

waves is negligible. To monitor any residual effect from the initial waves we repeat the calculation at two different evolution times. We will give more details on this procedure in Sec. IV B below.

D. Extrapolation to zero step size

Obtaining $F^{\alpha l}_{\rm reg}$ with good accuracy requires calculating $[F^{\alpha l}_{\rm full}(x_0)]_\pm$ with an even better accuracy, which, in turn, requires evolving the field equations with a sufficiently fine grid. This can become very demanding computationally, especially for large l. To reduce computational cost we use a Richardson extrapolation to $h \to 0$. The idea is to extrapolate the value of $F^{\alpha l}_{\rm reg}$ (using a rational function) to the limit of vanishing step size, using a sequence of values obtained with progressively decreasing step sizes. Specifically, we employ the Bulirsch-Stoer method [43], which utilizes the sequence

$$h_i = \frac{1}{n_i}, \tag{39}$$

where $i = 1, 2, 3, \ldots$ and

$$n_i = \{2, 4, 6, 8, 12, \cdots\} \qquad (n_i = 2n_{i-2}). \tag{40}$$

Namely, we repeat the calculation of $F^{\alpha l}_{\rm reg}$ for all step sizes $h_1, h_2, \ldots, h_{i_{\rm max}}$, and then extrapolate the resulting series of values to $i \to \infty$ ($h \to 0$). To control the error in this procedure we introduce the estimator

$$\Delta^{\alpha l}[i_{\rm max}] \equiv 2 \left| \frac{F^{\alpha l}_{\rm reg}[i_{\rm max}] - F^{\alpha l}_{\rm reg}[i_{\rm max} - 1]}{F^{\alpha l}_{\rm reg}[i_{\rm max}] + F^{\alpha l}_{\rm reg}[i_{\rm max} - 1]} \right|, \tag{41}$$

where $F^{\alpha l}_{\rm reg}[i_{\rm max}]$ is the value extrapolated from the sequence of $i_{\rm max}$ values of $F^{\alpha l}_{\rm reg}$ obtained with $h_1, \ldots, h_{i_{\rm max}}$. We repeat our calculation with increasing values of $i_{\rm max}$, until $\Delta^{\alpha l}[i_{\rm max}]$ is smaller than a prescribed threshold, $\Delta^{\alpha l}_{\rm thresh}$.

What value should $\Delta^{\alpha l}_{\rm thresh}$ be set to? This requires some consideration. Since the contribution to the mode sum from individual l modes decreases with l (at large l), it makes sense to relax the threshold for large l modes. This is certainly true for the t component, for which the mode sum converges *exponentially* at large l. Accordingly, for the t component we set the tight threshold $\Delta^{tl}_{\rm thresh} = 10^{-4}$ for each of the modes $l \le 3$, but for $l > 3$ we set $\Delta^{tl}_{\rm thresh} = 10^{-4} \times |(\sum_{l'=0}^{l-1} F^{tl'}_{\rm reg})/F^{t,l-1}_{\rm reg}|$. This is slightly larger than 10^{-4} for $l = 4$, but grows exponentially at large l. Experimentally, it yields $\Delta^{tl}_{\rm thresh} \sim 1$ for $l = 5$–9 (depending on r_0: higher l for smaller r_0). In fact, for the t component we use $\Delta^{tl}_{\rm thresh}$ also as an indicator to tell us when it is appropriate to terminate the sum over modes: We sum up to the first l mode for which $\Delta^{tl}_{\rm thresh} > 1$. This guarantees an overall truncation error less than a few $\times 10^{-4}$ in the t component of the SF. As for the r component: Here the mode sum converges only as $\sim l^{-2}$, and determining $\Delta^{rl}_{\rm thresh}$ requires more caution. As we describe below, we estimate the contribution from the truncated $l > 15$ tail by extrapolating the numerical data from $l \le 15$; assigning an l-dependent threshold could make it difficult to control the error from such an estimation. For the r component we therefore conservatively set a fixed threshold of $\Delta^{rl}_{\rm thresh} = 10^{-2}$ for each individual l mode computed.

For both r and t components, we estimate the overall (fractional) discretization error in the SF as

$$\Delta^{\alpha}_{\rm discr} \sim \frac{\sum_{l=0}^{l_{\rm max}} |\Delta^{\alpha l}[i_{\rm thresh}] F^{\alpha l}_{\rm reg}[i_{\rm thresh}]|}{|\sum_{l=0}^{l_{\rm max}} F^{\alpha l}_{\rm reg}[i_{\rm thresh}]|}, \tag{42}$$

where $i_{\rm thresh}$ (depending on l and r_0) is the smallest $i_{\rm max}$ for which $\Delta^{\alpha l}[i_{\rm max}] < \Delta^{\alpha l}_{\rm thresh}$. Note that we take here the fractional total error as the *sum* of fractional errors from the individual l-modes, rather than their root-mean-square value. This makes sense because the individual errors are not randomly distributed but rather reflect a systematic extrapolation error. In practice, to reach the above thresholds, we needed $i_{\rm thresh}$ values of up to 8 for the r component, and up to 9 for the t component (depending on l and r_0: larger $i_{\rm thresh}$ is generally required for larger l and smaller r_0).

For each value of r_0 and l we started the above procedure with $i_{\rm max} = 4$ for the r component and $i_{\rm max} = 3$ for the t component; namely, we used at least 4(3) terms for the Richardson extrapolation. For some of the low-l modes this already yielded $\Delta^{\alpha l}[i_{\rm max}]$ smaller than $\Delta^{\alpha l}_{\rm thresh}$ (this is partly because the low-l modes have large $l = 0$, 1 tensorial-harmonic components, which are available analytically). Since the total error $\Delta^{\alpha}_{\rm discr}$ is dominated by errors from these low-l modes, we generally find $\Delta^{\alpha}_{\rm discr}$ values *much smaller* than the above set thresholds. The actual values obtained for $\Delta^{\alpha}_{\rm discr}$ will be stated in the Results section.

E. Estimation of contribution from large-l tail

The mode-sum formula requires summation over all regularized modes $F^{\alpha l}_{\rm reg}$ from $l = 0$ to $l = \infty$. In practice, of course, we calculate only a finite number of modes, $0 \le l \le l_{\rm max}$. It is then necessary to estimate the contribution from the remaining, truncated part of the series. This is straightforward in the case of the t component, where the mode sum converges exponentially, and thus the contribution from the truncated tail drops exponentially with $l_{\rm max}$. We find experimentally that it is sufficient to take $l_{\rm max} =$ 4–9 (depending on r_0; larger $l_{\rm max}$ is needed for smaller r_0) for the contribution from the truncated tail to drop below our standard discretization error ($\sim 10^{-4}$).

The situation is different with the r component, where the mode sum converges as $\propto l^{-2}$, and the contribution from the truncated high-l tail scales as $1/l_{\rm max}$. For computationally realistic values of $l_{\rm max}$ (here we take $l_{\rm max} = 15$) this contribution cannot be neglected. To evaluate it we apply the following strategy. Let

$$F^r = F^r_{l\le l_{\max}} + F^r_{l>l_{\max}}, \tag{43}$$

where

$$F^r_{l\le l_{\max}} \equiv \sum_{l=0}^{l_{\max}} F^{rl}_{\rm reg} \quad \text{and} \quad F^r_{l>l_{\max}} \equiv \sum_{l=l_{\max}+1}^{\infty} F^{rl}_{\rm reg}. \tag{44}$$

The part $F^r_{l\le l_{\max}}$ is computed numerically. To evaluate $F^r_{l>l_{\max}}$ we extrapolate the last few modes in $F^r_{l\le l_{\max}}$ using the fitting formula

$$F^{rl}_{\rm reg} \simeq \sum_{n=1}^{N} \frac{D^r_{2n}}{L^{2n}} \tag{45}$$

(for some $N \ge 1$), where, recall, $L = l + 1/2$, and D^r_{2n} are l-independent coefficients, which serve here as fitting parameters. In practice we have used the last 6 modes of $F^r_{l\le l_{\max}}$ (i.e., $10 \le l \le 15$) for the fitting, but have checked that fitting using a different number of modes does not change the result significantly (we demonstrate this below). Given the coefficients D^r_{2n}, the large-l tail is estimated as

$$\begin{aligned} F^r_{l>l_{\max}} &\simeq \sum_{n=1}^{N} D^r_{2n} \sum_{l=l_{\max}+1}^{\infty} L^{-2n} \\ &= \sum_{n=1}^{N} \frac{D^r_{2n}}{(2n-1)!} \Psi(2n-1, l_{\max}+3/2), \end{aligned} \tag{46}$$

where $\Psi(n, x)$ is the polygamma function of order n, defined as

$$\Psi(n, x) = \frac{d^{n+1}[\log\Gamma(x)]}{dx^{n+1}}, \tag{47}$$

in which $\Gamma(x)$ is the standard gamma function.

To determine how many terms it is necessary to include in the fitting formula (45) requires some experimentation. The data in Table I demonstrates the effect of varying N: It shows the values obtained for $F^r_{l>l_{\max}}$ (both external and internal values) using N in the range 1–4. We display data for the two sample radii $r_0 = 6M$ and $r_0 = 100M$. We find that taking $N = 3$ or $N = 4$ gives the same value of $F^r_{l>l_{\max}}$ as taking $N = 2$, with a fractional difference of merely $\lesssim 10^{-4}$ at most. Since $F^r_{l>l_{\max}}$ itself contributes at most $\sim 2\%$ of the total force (see Tables VI and VII in Appendix D), we conclude that it is sufficient to take $N = 2$. Taking only $N = 1$ would produce a fitting error similar in magnitude to $\Delta^\alpha_{\rm discr}$; so, taking $N = 2$ effectively eliminates the large-l fitting as a source of error in our calculation. We find similar numbers for other values of r_0, and so we take $N = 2$ in all cases.

As a further robustness test for the above scheme, we check how the estimation of $F^r_{l>l_{\max}}$ would change by using higher multipole modes for the fitting. For this, we calculated numerically all modes up to $l = 25$ for $r_0 = 6M, 100M$. Results from this experiment are shown in Table II. Once again we take $F^r_{l>l_{\max}}$ as the sum of all modes $l > 15$, but this time we obtain the fitting parameters D_{2n} based on all *sixteen* modes $10 \le l \le 25$. Again, we check how the results depend on N. We find that the relative difference in the value of $F^r_{l>l_{\max}}$ with respect to our reference case [$N = 2$ and fitting based on $10 \le l \le 15$] is $\lesssim 10^{-4}$ in all cases, as long as we take $N \ge 2$. This reassures us that it is sufficient to base the fitting on $10 \le l \le 15$, as we do in the rest of this analysis.

Results from the above fitting procedure (with $N = 2$ and $10 \le l \le 15$) are illustrated in Fig. 4 for $r_0 = 6M$. As

TABLE I. Data demonstrating how sensitive the estimation of the large-l contribution is to the number of terms N included in the fitting formula (45). We display here results for the strong-field case ($r_0 = 6M$) and for the weak-field case ($r_0 = 100M$), and in both cases use the six numerically computed modes $10 \le l \le 15$ to fit for the part of the mode sum with $l > 15$. $[F^r_{l>15}]_-$ and $[F^r_{l>15}]_+$ are the estimated contributions from $l > 15$, obtained using internal and external data, respectively. For convenience, the values of $[F^r_{l>15}]_\pm$ are given multiplied by $10^4(M/\mu)^2$ for $r_0 = 6M$, and by $10^8(M/\mu)^2$ for $r_0 = 100M$. Values in square brackets indicate the fractional fitting error in $[F^r_{l>15}]_\pm$. The values in the 3rd and 5th columns show the relative differences in $[F^r_{l>15}]_\pm$ with respect to the reference case $N = 2$, which we adopt in the rest of this work. Note that the differences indicated are relative to the large-l contribution $[F^r_{l>15}]_\pm$ only; the differences relative to the total SF are at least 2 orders of magnitude smaller.

N	$[F^r_{l>15}]_-$ (fit using $10 \le l \le 15$)	Relative difference w.r.t. $N = 2$	$[F^r_{l>15}]_+$ (fit using $10 \le l \le 15$)	Relative difference w.r.t. $N = 2$
$r_0 = 6M$				
1	$-5.117\,158\ [2\times10^{-3}]$	-1.4×10^{-2}	$-5.117\,176\ [2\times10^{-3}]$	-1.4×10^{-2}
2	$-5.046\,144\ [3\times10^{-5}]$	0	$-5.046\,189\ [3\times10^{-5}]$	0
3	$-5.046\,984\ [6\times10^{-5}]$	-1.7×10^{-4}	$-5.046\,812\ [2\times10^{-4}]$	-1.2×10^{-4}
4	$-5.046\,316\ [4\times10^{-4}]$	-3.4×10^{-5}	$-5.046\,133\ [9\times10^{-4}]$	-1.1×10^{-5}
$r_0 = 100M$				
1	$-5.904\,165\ [1\times10^{-3}]$	-7.5×10^{-3}	$-5.904\,159\ [1\times10^{-3}]$	-7.5×10^{-3}
2	$-5.859\,951\ [2\times10^{-5}]$	0	$-5.859\,925\ [2\times10^{-5}]$	0
3	$-5.860\,397\ [8\times10^{-6}]$	-7.6×10^{-5}	$-5.860\,450\ [6\times10^{-6}]$	-9.0×10^{-5}
4	$-5.860\,430\ [7\times10^{-5}]$	-8.2×10^{-5}	$-5.860\,380\ [5\times10^{-5}]$	-7.8×10^{-5}

TABLE II. Data demonstrating how sensitive the estimation of the high-l contribution is to the number of modes used for the high-l fitting. The structure of this table is the same as that of Table I. Again we show data for $r_0 = 6M$ and $r_0 = 100M$, and $[F^r_{l>15}]_\pm$ describes the contribution from $l > 15$; however, we now use all 16 modes $10 \le l \le 25$ for fitting. The values in the 3rd and 5th columns show the relative differences with respect to the reference case, i.e., $N = 2$ and fitting using $10 \le l \le 15$—the case displayed in Table I. This demonstrates that, taking $N = 2$, it is sufficient to base our large-l fitting on data from $10 \le l \le 15$.

N	$[F^r_{l>15}]_-$ (fit using $10 \le l \le 25$)	Relative difference w.r.t. reference case	$[F^r_{l>15}]_+$ (fit using $10 \le l \le 25$)	Relative difference w.r.t. reference case
$r_0 = 6M$				
1	$-5.106\,648\ [1 \times 10^{-3}]$	-1.2×10^{-2}	$-5.106\,701\ [1 \times 10^{-3}]$	-1.2×10^{-2}
2	$-5.046\,340\ [2 \times 10^{-5}]$	-3.9×10^{-5}	$-5.046\,533\ [3 \times 10^{-5}]$	-6.8×10^{-5}
3	$-5.046\,634\ [3 \times 10^{-5}]$	-9.7×10^{-5}	$-5.046\,985\ [4 \times 10^{-5}]$	-1.6×10^{-4}
4	$-5.046\,500\ [1 \times 10^{-4}]$	-7.1×10^{-5}	$-5.047\,089\ [1 \times 10^{-4}]$	-1.8×10^{-4}
5	$-5.046\,769\ [4 \times 10^{-4}]$	-1.2×10^{-4}	$-5.047\,224\ [5 \times 10^{-4}]$	-2.1×10^{-4}
$r_0 = 100M$				
1	$-5.897\,633\ [8 \times 10^{-4}]$	-6.4×10^{-3}	$-5.897\,625\ [8 \times 10^{-4}]$	-6.4×10^{-3}
2	$-5.860\,129\ [1 \times 10^{-5}]$	-3.0×10^{-5}	$-5.860\,106\ [1 \times 10^{-5}]$	-3.1×10^{-5}
3	$-5.860\,367\ [7 \times 10^{-6}]$	-7.1×10^{-5}	$-5.860\,349\ [8 \times 10^{-6}]$	-7.2×10^{-5}
4	$-5.860\,371\ [2 \times 10^{-5}]$	-7.2×10^{-5}	$-5.860\,304\ [2 \times 10^{-5}]$	-6.5×10^{-5}
5	$-5.860\,407\ [9 \times 10^{-5}]$	-7.8×10^{-5}	$-5.860\,308\ [1 \times 10^{-4}]$	-6.5×10^{-5}

an indicative measure of the calculation error in $F^r_{l>l_{\max}}$ we take the standard (fractional) fitting error [43], which we denote $\Delta_{\rm tail}$. At least in the examples shown in Tables I and II, this has roughly the same magnitude as the error from changing the fitting method, so $\Delta_{\rm tail}$ provides a realistic estimate of the total (fractional) error in determining the tail contribution $F^r_{l>l_{\max}}$. The *relative* error from determining the large-l tail, expressed as a fraction of the total SF, is

$$\Delta_{\rm tail,rel} = \Delta_{\rm tail} \times \left| \frac{F^r_{l>l_{\max}}}{F^r_{l\le l_{\max}}} \right|. \tag{48}$$

In practice we find (see Appendix D) $F^r_{l>l_{\max}}/F^r_{l\le l_{\max}} \sim 10^{-2}$–$10^{-4}$ for r_0 in the range $6M$–$150M$. The relative fitting error $\Delta_{\rm tail,rel}$ is a mere $\sim 7 \times 10^{-5}$ at $r_0 = 6M$, dropping down to $\sim 2 \times 10^{-7}$ at $r_0 = 150M$.

IV. CODE VALIDATION

A few validation tests for our metric perturbation code were presented in BL. These included (i) a demonstration that the numerical solutions for the various $\bar{h}^{(i)lm}$'s converge quadratically as $h \to 0$; (ii) a demonstration that these solutions satisfy the Lorenz-gauge conditions; (iii) a confirmation that the flux of energy radiated to null infinity in the various modes, as calculated from our Lorenz-gauge solutions, compares well with the flux obtained using other methods/gauges. Here we present some more validation tests, focusing on the new ingredient of the

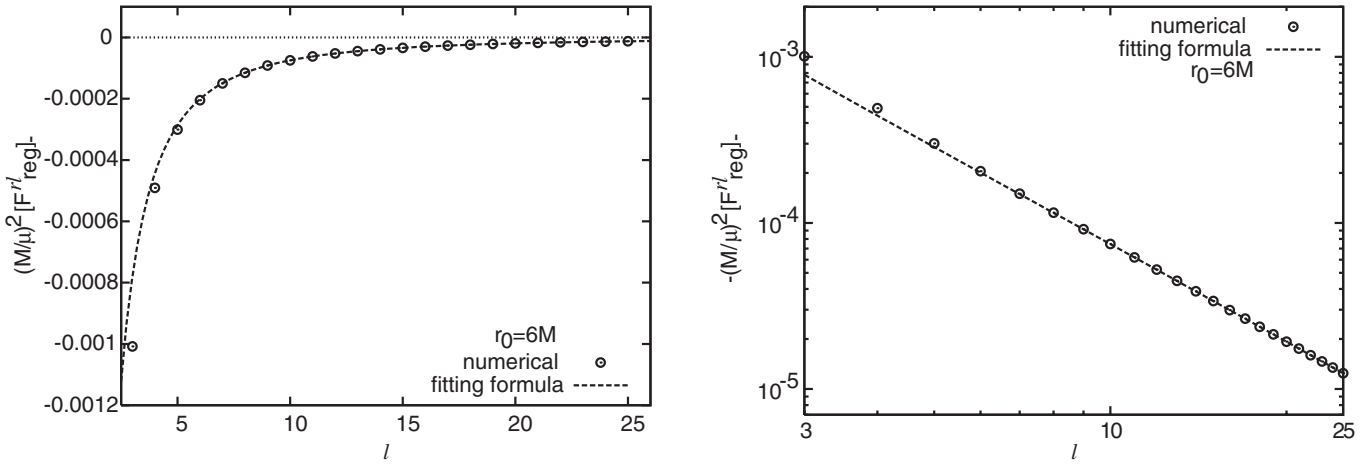

FIG. 4. Analytic fitting for the large-l tail of the SF, exemplified here for $r_0 = 6M$. We used the fitting formula (45) with $N = 2$, and based on the modes $10 \le l \le 15$. Circles ("⊙") represent actual data obtained for $F^{rl}_{\rm reg}$ (calculated from r_0^-), for the various modes $3 \le l \le 25$. The dashed line is the analytic fit. Left/right panels show the same data on linear/log scales. The large-l tail of the mode-sum series shows the l^{-2} falloff expected from theory (cf. Fig. 7).

analysis, i.e., the calculation of the SF. We will demonstrate (i) quadratic numerical convergence of the computed SF; (ii) that the SF does not depend on our choice of initial data; (iii) that the full-force modes have large-l behavior as predicted in theory [Eq. (20)]; (iv) that the two one-sided values obtained for the final SF (from r_0^+ and from r_0^-) agree; and (v) that the total flux of energy to infinity and through the horizon is consistent with the value obtained for the temporal component of the SF.

A. Numerical convergence

The scheme introduced in Sec. III should yield the final SF with a numerical error scaling as $\sim h^2$ (where h is the step size in both u and v). To check this, we performed the following test, for a selection of r_0 values in the range $6M$–$150M$ and l values in the range 0–15. For given r_0 and l we calculated the regularized mode $F^{rl}_{\rm reg}$ through the scheme described in Sec. III (including the extrapolation to $h \to 0$). We recorded the values of the force calculated with the different resolutions h_i [see Eq. (39)]. Denoting these by $F^{rl}_{\rm reg}[h_i]$, we then plotted the difference $F^{rl}_{\rm reg}[h_i] - F^{rl}_{\rm reg}$ (where the second term is the extrapolated force) as a function of h_i. Figure 5 shows the two modes $l = 2$, 15 at $r_0 = 6M$. In each case we plot both one-sided values of the difference $F^{rl}_{\rm reg}[h_i] - F^{rl}_{\rm reg}$. In all cases we find that this difference decreases approximately like h^2 at small h, demonstrating quadratic numerical convergence. Similar convergence is observed for the t component.

B. Dependence on initial conditions

As explained above, we start the evolution of each of the modes $\bar{h}^{(i)lm}$ with null values along the initial surfaces, $v = v_0$ and $u = u_0$. This creates a "spark" of spurious radiation which propagates through the grid, but dies off at late time. During the early transient period the numerical solution is not stationary; as the spurious waves die off, the numerical solution approaches its physical, stationary value. This behavior is demonstrated in the plots in Fig. 6. The SF has to be calculated at late enough time, to assure that the error due to residual initial waves is negligible. This sets a lower limit on the required evolution time $T_{\rm evo}$, which in practice depends on r_0: Waves from an initial spark at $r_0 = 100M$ dissipate more efficiently (faster) than waves from an initial spark at $r_0 = 6M$, since the former experience less scattering off spacetime curvature.

In our analysis we determined $T_{\rm evo}$ experimentally, for each value of r_0 considered. To assess the effect of residual waves, we compared the values obtained for the final SF at two different evolution times, $T_{\rm evo}$ and $0.8 \times T_{\rm evo}$. We regard this difference as indicative of the error from non-stationarity in our calculation. The errors calculated for the various values of r_0 are shown in Tables IV and V of Sec. V below. The fractional error is smaller than 10^{-4} in all cases, hence smaller than our standard discretization error. Table III lists the evolution times $T_{\rm evo}(r_0)$ used in our analysis.

C. Large l behavior of the full-force modes

The fact that our numerically derived full modes $[F^{\alpha l}_{\rm full}(x_0)]_\pm$ exhibit the right behavior at large l, through *three* leading terms in the $1/L$ expansion [$O(L)$ to $O(1/L)$] provides a very strong quantitative check on our code. The plots in Fig. 7 demonstrate that the regularized modes $F^{\alpha l}_{\rm reg} \equiv [F^{\alpha l}_{\rm full}(x_0)]_\pm - A^\alpha_\pm L - B^\alpha$ fall off faster than $1/l$ at

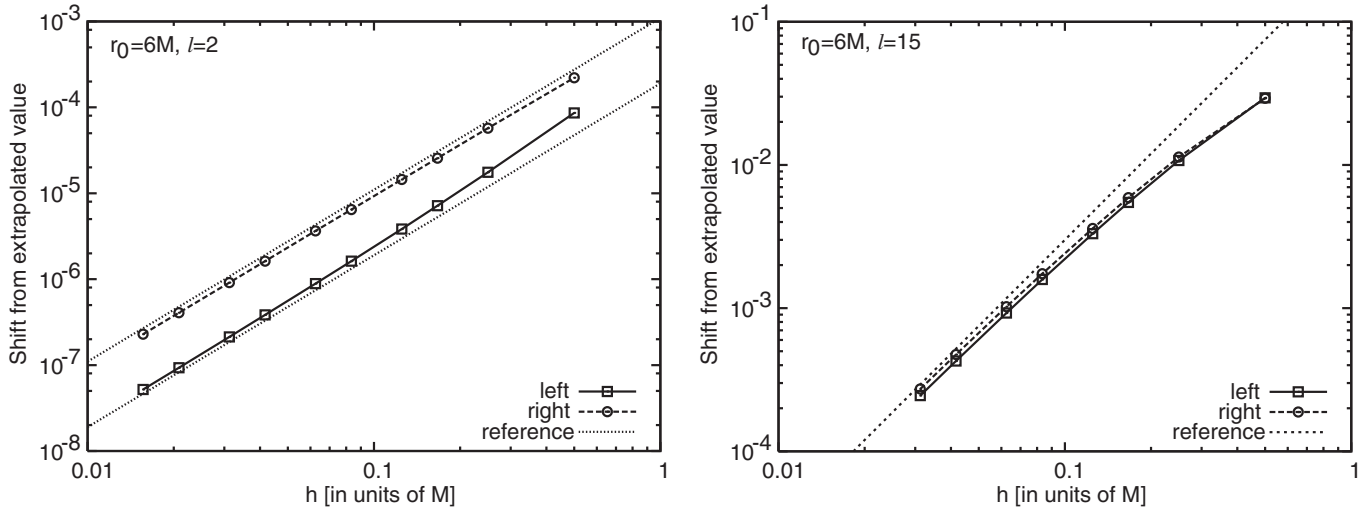

FIG. 5. Numerical convergence of the calculated SF, demonstrated here for the r component, for $r_0 = 6M$. The left and right panels show $l = 2$ and $l = 15$, respectively. Plotted is the difference $F^{rl}_{\rm reg}[h_i] - F^{rl}_{\rm reg}$ between the value of the regularized mode computed with step size h_i, and the value extrapolated to $h \to 0$. Each panel displays both one-sided values of the force: "left" and "right" stand for r_0^- and r_0^+ values, respectively. The reference lines (dotted) have slopes $\propto h^2$. This demonstrates the quadratic convergence of the numerical calculation.

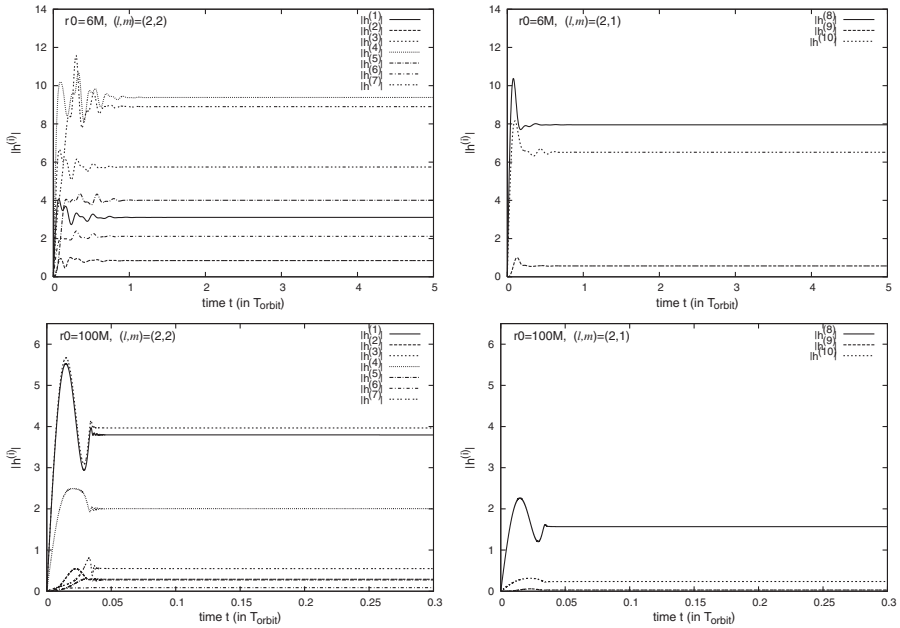

FIG. 6. Time evolution of the metric perturbation. We plot the absolute values of the various functions $\bar{h}^{(i)lm}$, evaluated at the location of the particle, as a function of t, for $l = 2$ and $m = 1, 2$. Top two figures are for $r_0 = 6M$; lower two figures are for $r_0 = 100M$. The time t is indicated along the horizontal axis in units of the orbital period, $T_{\rm orb}$. The initial transient phase is due to the imperfection of the initial conditions; these spurious waves dissipate rapidly, clearing the stage for the physical, stationary solution. The SF is calculated at late time, when the effect of the initial spurious waves is negligible.

large l: The r component falls off as $\sim L^{-2}$, and the t component falls off exponentially. For the r component this indicates that the "singular" (large l) part of the calculated full modes is correctly described by the analytic regularization function $A^r_{\pm}L + B^r$, through $O(1/L)$. Of course, this agreement is necessary for a successful implementation of the mode-sum formula: If the modes $[F^{rl}_{\rm full}(x_0)]_{\pm}$ were inconsistent with the regularization function, the sum over modes would diverge. Note also that the procedure for evaluating the large l tail (Sec. III E) relies on the computed modes having the correct behavior at large l.

TABLE III. Evolution times taken in our analysis. These were chosen (experimentally) long enough to guarantee that any residual effect from the initial spurious waves is negligible. $T_{\rm evo}$ is the numerical evolution time, and $T_{\rm orb} = 2\pi/\Omega_0$ is the orbital period.

r_0/M	$T_{\rm evo}/T_{\rm orb}$ (r component)	$T_{\rm evo}/T_{\rm orb}$ (t component)
6–10	3	3
11–12	2.5	2.8
13–14	2	2.8
15	1.5	2.5
20	1	2
30	0.8	1.8
40	0.6	1.7
50	0.5	1.5
60	0.45	1.5
70	0.4	1.2
80	0.3	1.0
90	0.25	1.0
100	0.2	0.8
120	0.15	0.8
150	0.12	0.6

D. Agreement between one-sided values of the SF

In this analysis we applied the standard version of the mode-sum formula, Eq. (20), rather than the "averaged" version, Eq. (23). For the r component we carried out two independent calculations of the SF, once using the internal values $[F^{rl}_{\rm full}(x_0)]_-$, and again using the external values $[F^{rl}_{\rm full}(x_0)]_+$. (The two one-sided values of the t component coincide automatically, as the full modes of this component are continuous at the worldline.) This allows for an important consistency check: The external and internal values of the final SF must agree. Any difference between the two values is due to numerical error. Denoting the computational difference between external and internal values of the final SF by $\Delta_{\pm}$, we find experimentally

$$\Delta_{\pm}/F^r \sim 10^{-5}\text{–}10^{-9} \tag{49}$$

(depending on r_0). This is well under the numerical error from discretization. The experimental values of $\Delta_{\pm}$, for the different orbital radii considered, can be found in Table IV of Sec. V.

E. Energy balance

Equation (7) relates the temporal component of the SF to the momentary rate of change of the (specific) orbital

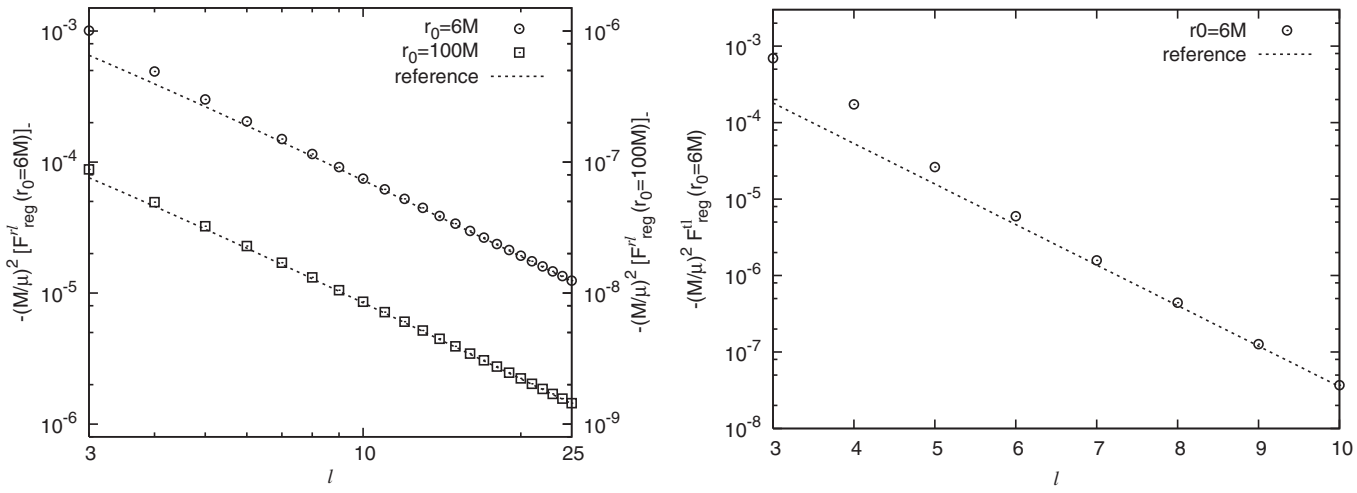

FIG. 7. Large-l behavior of the regularized modes $F^{\alpha l}_{\rm reg}$. The reference lines in the left panel are $\propto l^{-2}$; the reference line in the right panel is $\propto \exp(-1.22l)$. The left panel displays the radial component $F^{rl}_{\rm reg}$ (calculated using internal derivatives) for $3 \leq l \leq 25$ and for $r_0 = 6M$, $100M$. The regularized modes appear to fall off as $\propto l^{-2}$ at large l, in agreement with theory. The right panel shows the l-modes of the t component (for $r_0 = 6M$); these are already regularized, and show an exponential falloff at large l. (Note the scale for the two panels is different: log-log for the left panel, semilog for the right.)

energy parameter $\mathcal{E}$. In terms of time t, this relation becomes $\dot{\mathcal{E}} = -(\mu u^t_0)^{-1} F_t$, where an overdot denotes d/dt, and $u^t_0 = (1 - 3M/r_0)^{-1/2}$. If we assume that μ/M is small enough that radiation reaction is negligible over an orbital period $T_{\rm orb}$ ("adiabatic approximation"), then, for a circular orbit, $\dot{\mathcal{E}}$ also represents the average rate of change of $\mathcal{E}$ over $T_{\rm orb}$. This must be balanced by the flux of gravitational-wave energy radiated to infinity and through the horizon, averaged over $T_{\rm orb}$. If we denote the former by $\dot{E}_\infty$ and the latter by $\dot{E}_{\rm EH}$ (both taken positive), we have the energy-balance formula

$$\dot{E}_{\rm total} \equiv \dot{E}_\infty + \dot{E}_{\rm EH} = -\mu\dot{\mathcal{E}} = F_t/u^t_0. \tag{50}$$

Both asymptotic fluxes $\dot{E}_\infty$ and $\dot{E}_{\rm EH}$ can be constructed from the perturbation fields $\bar{h}^{(i)lm}$, evaluated at the corresponding asymptotic domains. Validity of Eq. (50) then provides a strong qualitative test of our calculation.

We can readily express the asymptotic fluxes $\dot{E}_\infty$ and $\dot{E}_{\rm EH}$ in terms of the $\bar{h}^{(i)lm}$'s, with the help of the Weyl scalars, $\psi_0 = -C_{\alpha\beta\gamma\delta} l^\alpha m^\beta l^\gamma m^\delta$ and $\psi_4 = -C_{\alpha\beta\gamma\delta} n^\alpha \times m^{*\beta} n^\gamma m^{*\delta}$. Here $C_{\alpha\beta\gamma\delta}$ is the Weyl tensor corresponding to the perturbation $h_{\alpha\beta}$, and l^α, n^α, and m^α are the Kinnersley null vectors, given by $l^\alpha = (f^{-1}, 1, 0, 0)$ $n^\alpha = \frac{1}{2}(1, -f, 0, 0)$, and $m^\alpha = \frac{1}{\sqrt{2}r}(0, 0, 1, \frac{i}{\sin\theta})$. Decomposing the perturbation as in Eq. (16), we obtain the asymptotic relations

$$\psi_4(r \to \infty) = \sum_{l=2}^{\infty} \sum_{m=-l}^{l} \frac{1}{4l(l+1)\lambda r} (\ddot{\bar{h}}^{(7)} + i\ddot{\bar{h}}^{(10)})[D_2 Y_{lm} - i(\sin\theta)^{-1} D_1 Y_{lm}],$$

$$\psi_0(r \to 2M) = \sum_{l=2}^{\infty} \sum_{m=-l}^{l} \frac{1}{4(2M)^3 f^2} \Big\{ \bar{h}^{(1)} + \bar{h}^{(2)} + \frac{\bar{h}^{(4)} + \bar{h}^{(5)} - i(\bar{h}^{(8)} + \bar{h}^{(9)})}{l(l+1)} - \frac{4M}{l(l+1)} [\dot{\bar{h}}^{(4)} + \dot{\bar{h}}^{(5)} - i(\dot{\bar{h}}^{(8)} + \dot{\bar{h}}^{(9)})]$$
$$- \frac{4M}{l(l+1)\lambda} [\dot{\bar{h}}^{(7)} - i\dot{\bar{h}}^{(10)} - 4M(\ddot{\bar{h}}^{(7)} - i\ddot{\bar{h}}^{(10)})] \Big\} (D_2 Y_{lm} + i(\sin\theta)^{-1} D_1 Y_{lm}). \tag{51}$$

The first relation is valid at leading order in $1/r$, and the second at leading order in f. In obtaining these relations we have made the replacements $f\partial_r \to -\partial_t$ (for ψ_4 at null infinity) and $f\partial_r \to \partial_t$ (for ψ_0 at the horizon). For circular orbits, the asymptotic fluxes are given in terms of the Weyl scalars as [44,45]

$$\dot{E}_\infty = \int d\tilde{\Omega} \frac{r^2}{4\pi m^2 \Omega_0^2} |\psi_4(r \to \infty)|^2, \tag{52}$$

$$\dot{E}_{\rm EH} = \int d\tilde{\Omega} \frac{M^4 f^4}{\pi(1 + 16M^2 m^2 \Omega_0^2)} |\psi_0(r \to 2M)|^2, \tag{53}$$

where the integration is carried out over 2-spheres $r = {\rm const} \to \infty$ and $r = 2M$, respectively. Now proceed as follows: (i) Substitute Eqs. (51) in Eqs. (52). (ii) For $\dot{E}_{\rm EH}$ apply the asymptotic gauge conditions $\bar{h}^{(2)} = \bar{h}^{(1)}$, $\bar{h}^{(4)} = \bar{h}^{(5)}$, and $\bar{h}^{(8)} = \bar{h}^{(9)}$ [see Eqs. (A13)–(A16) in Appendix A]. (iii) Replace $d/dt \to -im\Omega_0$. (iv) Integrate

over the spheres using the formulas (A4) of BL. This yields the final relations

$$\dot{E}_\infty = \sum_{l=2}^{\infty} \sum_{m=-l}^{l} \frac{\mu^2 m^2 \Omega_0^2}{64\pi\lambda l(l+1)} |\bar{h}_\infty^{(7)} - i\bar{h}_\infty^{(10)}|^2, \tag{54}$$

$$\dot{E}_{\rm EH} = \sum_{l=2}^{\infty} \sum_{m=-l}^{l} \frac{\mu^2 \lambda l(l+1)}{256\pi M^2(1+16M^2m^2\Omega_0^2)} \times \left| \bar{h}_{\rm EH}^{(1)} + \frac{1+4iMm\Omega_0}{l(l+1)} [\bar{h}_{\rm EH}^{(5)} - i\bar{h}_{\rm EH}^{(9)} + 2iMm\Omega_0\lambda^{-1}(\bar{h}_{\rm EH}^{(7)} - i\bar{h}_{\rm EH}^{(10)})] \right|^2, \tag{55}$$

where $\lambda = (l-1)(l+2)$, $\bar{h}_\infty^{(i)}$ are the fields $\bar{h}^{(i)lm}$ evaluated at null infinity ($u \ll v \to \infty$), and $\bar{h}_{\rm EH}^{(i)}$ are these fields evaluated at the event horizon ($v \ll u \to \infty$). Equation (54) for $\dot{E}_\infty$ agrees with Eq. (57) of BL, which was derived directly from the Issacson effective energy-momentum tensor.

To test our calculation of F_t, we used our evolution code to obtain the energy fluxes at infinity and through the horizon, based on Eqs. (54) and (55), and then checked consistency with the balance Eq. (50). To extract $\dot{E}_\infty$ we evaluated the numerical solutions $\bar{h}^{(7,10)}$ at $v = 5200M$, $9000M$, $15\,000M$ and $u = 800M$, $3000M$, $5000M$, for orbital radii in the ranges $6M \le r_0 < 20M$, $20M \le r_0 \le 100M$, and $r_0 > 100M$, respectively. To derive $\dot{E}_{\rm EH}$ we evaluated $\bar{h}^{(1,5,7,9,10)}$ at $u = 5200M$, $6500M$, $7500M$ and $v = 800M$, $1500M$, $2500M$ for the above corresponding values of r_0. These values were selected experimentally such that the fractional error in the total flux (from the finite

TABLE IV. Final results for the radial component of the SF. The second column lists the values obtained for the various orbital radii r_0, taken as the average between internal and external values: $([F^r]_+ + [F^r]_-)/2$. Values in square brackets in the second column are estimates of the fractional numerical error in F^r from the finite-grid discretization (see the text for details). The third and fourth columns display estimates of the magnitude of error from two other sources: The third column shows the magnitude of the difference $[F^r]_+ - [F^r]_-$, which is entirely due to numerical error; the values in square brackets give the fractional error $2([F^r]_+ - [F^r]_-)/([F^r]_+ + [F^r]_-)$. The fourth column shows the estimated error from residual nonstationarity of the late-time numerical evolution, which is mainly due to leftover spurious waves arising from the imperfect initial data; values in square brackets again describe the fractional error. Both sources of error contribute negligibly to the overall error in the SF, which is therefore dominated by the discretization error.

r_0/M	$F^r \times (M/\mu)^2$	Error from disagreement $[F^r]_+ \leftrightarrow [F^r]_-$	Error from nonstationarity
6.0	$2.446\,61 \times 10^{-2}$ $[9 \times 10^{-4}]$	1.20×10^{-7} $[5 \times 10^{-6}]$	1.83×10^{-8} $[7 \times 10^{-7}]$
6.2	$2.396\,51 \times 10^{-2}$ $[9 \times 10^{-4}]$	5.01×10^{-9} $[2 \times 10^{-7}]$	5.92×10^{-8} $[2 \times 10^{-6}]$
6.4	$2.339\,54 \times 10^{-2}$ $[8 \times 10^{-4}]$	8.54×10^{-8} $[4 \times 10^{-6}]$	3.91×10^{-8} $[2 \times 10^{-6}]$
6.6	$2.278\,29 \times 10^{-2}$ $[7 \times 10^{-4}]$	1.56×10^{-7} $[7 \times 10^{-6}]$	4.24×10^{-8} $[2 \times 10^{-6}]$
6.8	$2.214\,62 \times 10^{-2}$ $[7 \times 10^{-4}]$	2.11×10^{-7} $[1 \times 10^{-5}]$	3.21×10^{-8} $[1 \times 10^{-6}]$
7.0	$2.149\,89 \times 10^{-2}$ $[6 \times 10^{-4}]$	2.42×10^{-7} $[1 \times 10^{-5}]$	2.64×10^{-8} $[1 \times 10^{-6}]$
7.2	$2.085\,04 \times 10^{-2}$ $[6 \times 10^{-4}]$	2.75×10^{-7} $[1 \times 10^{-5}]$	2.24×10^{-8} $[1 \times 10^{-6}]$
7.4	$2.020\,78 \times 10^{-2}$ $[6 \times 10^{-4}]$	3.02×10^{-7} $[1 \times 10^{-5}]$	1.93×10^{-8} $[1 \times 10^{-6}]$
7.6	$1.957\,61 \times 10^{-2}$ $[5 \times 10^{-4}]$	3.18×10^{-7} $[2 \times 10^{-5}]$	1.59×10^{-8} $[8 \times 10^{-7}]$
7.8	$1.895\,86 \times 10^{-2}$ $[5 \times 10^{-4}]$	3.28×10^{-7} $[2 \times 10^{-5}]$	1.32×10^{-8} $[7 \times 10^{-7}]$
8.0	$1.835\,77 \times 10^{-2}$ $[5 \times 10^{-4}]$	3.34×10^{-7} $[2 \times 10^{-5}]$	1.13×10^{-8} $[6 \times 10^{-7}]$
9.0	$1.563\,69 \times 10^{-2}$ $[4 \times 10^{-4}]$	3.23×10^{-7} $[2 \times 10^{-5}]$	5.70×10^{-9} $[4 \times 10^{-7}]$
10.0	$1.338\,95 \times 10^{-2}$ $[8 \times 10^{-5}]$	1.00×10^{-9} $[7 \times 10^{-8}]$	2.89×10^{-9} $[2 \times 10^{-7}]$
11.0	$1.155\,18 \times 10^{-2}$ $[6 \times 10^{-5}]$	1.55×10^{-9} $[1 \times 10^{-7}]$	1.49×10^{-11} $[1 \times 10^{-9}]$
12.0	$1.004\,63 \times 10^{-2}$ $[5 \times 10^{-5}]$	9.79×10^{-10} $[1 \times 10^{-7}]$	7.84×10^{-12} $[8 \times 10^{-10}]$
13.0	$8.804\,89 \times 10^{-3}$ $[4 \times 10^{-5}]$	3.38×10^{-9} $[4 \times 10^{-7}]$	1.96×10^{-9} $[2 \times 10^{-7}]$
14.0	$7.773\,07 \times 10^{-3}$ $[1 \times 10^{-5}]$	1.50×10^{-9} $[2 \times 10^{-7}]$	1.62×10^{-9} $[2 \times 10^{-7}]$
15.0	$6.908\,15 \times 10^{-3}$ $[3 \times 10^{-5}]$	1.17×10^{-9} $[2 \times 10^{-7}]$	1.25×10^{-9} $[2 \times 10^{-7}]$
20.0	$4.157\,06 \times 10^{-3}$ $[1 \times 10^{-5}]$	1.76×10^{-10} $[4 \times 10^{-8}]$	7.11×10^{-10} $[2 \times 10^{-7}]$
30.0	$1.969\,82 \times 10^{-3}$ $[5 \times 10^{-6}]$	8.39×10^{-11} $[4 \times 10^{-8}]$	2.86×10^{-10} $[1 \times 10^{-7}]$
40.0	$1.142\,88 \times 10^{-3}$ $[2 \times 10^{-6}]$	1.65×10^{-11} $[1 \times 10^{-8}]$	8.78×10^{-11} $[8 \times 10^{-8}]$
50.0	$7.449\,49 \times 10^{-4}$ $[1 \times 10^{-6}]$	3.03×10^{-12} $[4 \times 10^{-9}]$	4.98×10^{-11} $[7 \times 10^{-8}]$
60.0	$5.236\,13 \times 10^{-4}$ $[2 \times 10^{-5}]$	4.86×10^{-10} $[9 \times 10^{-7}]$	1.57×10^{-11} $[3 \times 10^{-8}]$
70.0	$3.880\,10 \times 10^{-4}$ $[1 \times 10^{-5}]$	2.47×10^{-10} $[6 \times 10^{-7}]$	1.79×10^{-12} $[5 \times 10^{-9}]$
80.0	$2.989\,79 \times 10^{-4}$ $[8 \times 10^{-6}]$	1.36×10^{-10} $[5 \times 10^{-7}]$	1.39×10^{-11} $[5 \times 10^{-8}]$
90.0	$2.374\,06 \times 10^{-4}$ $[7 \times 10^{-6}]$	8.01×10^{-11} $[3 \times 10^{-7}]$	1.58×10^{-11} $[7 \times 10^{-8}]$
100.0	$1.930\,63 \times 10^{-4}$ $[5 \times 10^{-6}]$	4.90×10^{-11} $[3 \times 10^{-7}]$	1.53×10^{-11} $[8 \times 10^{-8}]$
120.0	$1.348\,68 \times 10^{-4}$ $[4 \times 10^{-6}]$	2.17×10^{-11} $[2 \times 10^{-7}]$	1.22×10^{-12} $[9 \times 10^{-9}]$
150.0	$8.682\,74 \times 10^{-5}$ $[2 \times 10^{-6}]$	7.62×10^{-12} $[9 \times 10^{-8}]$	1.48×10^{-11} $[2 \times 10^{-7}]$

extraction distance and from the spurious initial waves) is less than 10^{-4} for each of the l modes. We then used these values in Eqs. (54) and (55), summing from $l = 2$ to $l = l_{\max}$, where $l_{\max}$ was determined experimentally, requiring that the fractional truncation error in the total flux (from omitting the modes $l > l_{\max}$) is $<10^{-4}$. This required $l_{\max}$ values between 9 (for $r_0 = 6M$) and 4 (for $r_0 = 150M$).

Following the above procedure, we obtained $\dot{E}_\infty$ and $\dot{E}_{\rm EH}$ for a list of orbital radii between $6M$ and $150M$. The ratio $\dot{E}_{\rm EH}/\dot{E}_\infty$ turns out very small for all radii, decreasing monotonically with r_0 from 3.3×10^{-3} at $r_0 = 6M$ to 2.4×10^{-9} at $r_0 = 150M$ (these values are consistent with Martel's [42]). The values obtained for the *total* energy flux, $\dot{E}_{\rm total} = \dot{E}_\infty + \dot{E}_{\rm EH}$, are listed in Table V of Sec. V below. We find that the fractional difference $|u_0^t \dot{E}_{\rm total}/F_t - 1|$ is less than $\sim 5 \times 10^{-4}$ in all cases, providing a strong quantitative check of our results.

V. RESULTS

A. Temporal component

We calculated the t component of the SF for 29 values of the orbital radius, in the range from $r_0 = 6M$ to $r_0 = 150M$, using the procedure described in Sec. III. The results are displayed in Table V. The computation error in F^t is estimated at $\lesssim 10^{-4}$ for all radii considered. The table also shows, for each of the radii considered, how the work done by the temporal component of the local SF is balanced by the total flux of radiated energy.

B. Radial component

We calculated the radial component of the SF for 29 values of the orbital radius, in the range from $r_0 = 6M$ to $t_0 = 150M$. Tables VI and VII in Appendix D present results for the internal and external values of the SF,

TABLE V. The temporal component of the SF, as a function of the orbital radius r_0. Values in the first square brackets in the second column are estimates of the *fractional* numerical error in F^t from the finite-grid discretization, $\Delta^t_{\rm discr}$ [see Eq. (42)]. Values in the second square brackets in the second column are estimates of the fractional error from residual nonstationarity of the late-time numerical evolution (which is mainly due to leftover spurious waves arising from the imperfect initial data). The third and fourth columns compare between the work done by the temporal SF and the total flux of energy radiated in gravitational waves, the latter extracted from the numerical solutions using the procedure described in Sec. IV E. The last column displays the relative difference $|\dot{E}_{\rm total}/(F_t/u_0^t) - 1|$, showing that the balance Eq. (50) is satisfied within the numerical accuracy, and providing a strong quantitative check of our results.

r_0/M	$(M/\mu)^2 F^t$	$(M/\mu)^2 F_t/u_0^t$	$(M/\mu)^2 \dot{E}_{\rm total}$	Rel. Diff.
6.0	$-1.994\,76 \times 10^{-3}$ [7×10^{-5}] [6×10^{-6}]	$9.403\,38 \times 10^{-4}$	$9.401\,90 \times 10^{-4}$	1.6×10^{-4}
6.2	$-1.605\,15 \times 10^{-3}$ [8×10^{-5}] [1×10^{-5}]	$7.811\,83 \times 10^{-4}$	$7.810\,64 \times 10^{-4}$	1.5×10^{-4}
6.4	$-1.305\,50 \times 10^{-3}$ [7×10^{-5}] [1×10^{-5}]	$6.541\,80 \times 10^{-4}$	$6.541\,01 \times 10^{-4}$	1.2×10^{-4}
6.6	$-1.071\,97 \times 10^{-3}$ [7×10^{-5}] [1×10^{-5}]	$5.517\,94 \times 10^{-4}$	$5.517\,23 \times 10^{-4}$	1.3×10^{-4}
6.8	$-8.878\,44 \times 10^{-4}$ [6×10^{-5}] [1×10^{-5}]	$4.684\,97 \times 10^{-4}$	$4.684\,11 \times 10^{-4}$	1.8×10^{-4}
7.0	$-7.411\,01 \times 10^{-4}$ [7×10^{-5}] [1×10^{-5}]	$4.001\,57 \times 10^{-4}$	$4.001\,17 \times 10^{-4}$	1.0×10^{-4}
7.2	$-6.230\,65 \times 10^{-4}$ [7×10^{-5}] [1×10^{-5}]	$3.436\,87 \times 10^{-4}$	$3.436\,27 \times 10^{-4}$	1.7×10^{-4}
7.4	$-5.272\,71 \times 10^{-4}$ [6×10^{-5}] [1×10^{-5}]	$2.966\,92 \times 10^{-4}$	$2.966\,45 \times 10^{-4}$	1.6×10^{-4}
7.6	$-4.489\,05 \times 10^{-4}$ [6×10^{-5}] [1×10^{-5}]	$2.573\,36 \times 10^{-4}$	$2.572\,88 \times 10^{-4}$	1.9×10^{-4}
7.8	$-3.843\,24 \times 10^{-4}$ [5×10^{-5}] [1×10^{-5}]	$2.241\,84 \times 10^{-4}$	$2.241\,48 \times 10^{-4}$	1.6×10^{-4}
8.0	$-3.307\,40 \times 10^{-4}$ [5×10^{-5}] [1×10^{-5}]	$1.961\,05 \times 10^{-4}$	$1.960\,66 \times 10^{-4}$	2.0×10^{-4}
9.0	$-1.668\,10 \times 10^{-4}$ [5×10^{-5}] [1×10^{-5}]	$1.059\,33 \times 10^{-4}$	$1.059\,08 \times 10^{-4}$	2.4×10^{-4}
10.0	$-9.190\,67 \times 10^{-5}$ [3×10^{-5}] [9×10^{-6}]	$6.151\,58 \times 10^{-5}$	$6.150\,47 \times 10^{-5}$	1.8×10^{-4}
11.0	$-5.416\,05 \times 10^{-5}$ [3×10^{-5}] [2×10^{-5}]	$3.779\,04 \times 10^{-5}$	$3.778\,56 \times 10^{-5}$	1.3×10^{-4}
12.0	$-3.365\,87 \times 10^{-5}$ [2×10^{-5}] [2×10^{-5}]	$2.429\,11 \times 10^{-5}$	$2.428\,57 \times 10^{-5}$	2.2×10^{-4}
13.0	$-2.183\,88 \times 10^{-5}$ [2×10^{-5}] [2×10^{-5}]	$1.620\,71 \times 10^{-5}$	$1.620\,22 \times 10^{-5}$	3.1×10^{-4}
14.0	$-1.468\,51 \times 10^{-5}$ [1×10^{-4}] [2×10^{-5}]	$1.115\,74 \times 10^{-5}$	$1.115\,64 \times 10^{-5}$	8.5×10^{-5}
15.0	$-1.017\,72 \times 10^{-5}$ [1×10^{-4}] [2×10^{-5}]	$7.889\,04 \times 10^{-6}$	$7.885\,97 \times 10^{-6}$	3.9×10^{-4}
20.0	$-2.255\,49 \times 10^{-6}$ [6×10^{-5}] [6×10^{-6}]	$1.871\,51 \times 10^{-6}$	$1.871\,11 \times 10^{-6}$	2.2×10^{-4}
30.0	$-2.808\,13 \times 10^{-7}$ [4×10^{-5}] [4×10^{-5}]	$2.486\,43 \times 10^{-7}$	$2.486\,00 \times 10^{-7}$	1.7×10^{-4}
40.0	$-6.512\,19 \times 10^{-8}$ [3×10^{-5}] [3×10^{-6}]	$5.950\,07 \times 10^{-8}$	$5.948\,97 \times 10^{-8}$	1.8×10^{-4}
50.0	$-2.108\,49 \times 10^{-8}$ [2×10^{-5}] [4×10^{-5}]	$1.962\,49 \times 10^{-8}$	$1.962\,03 \times 10^{-8}$	2.3×10^{-4}
60.0	$-8.413\,06 \times 10^{-9}$ [9×10^{-5}] [3×10^{-5}]	$7.926\,70 \times 10^{-9}$	$7.924\,24 \times 10^{-9}$	3.1×10^{-4}
70.0	$-3.874\,11 \times 10^{-9}$ [8×10^{-5}] [4×10^{-5}]	$3.681\,89 \times 10^{-9}$	$3.680\,86 \times 10^{-9}$	2.8×10^{-4}
80.0	$-1.980\,69 \times 10^{-9}$ [7×10^{-5}] [8×10^{-5}]	$1.894\,62 \times 10^{-9}$	$1.893\,60 \times 10^{-9}$	5.4×10^{-4}
90.0	$-1.096\,54 \times 10^{-9}$ [6×10^{-5}] [6×10^{-5}]	$1.054\,15 \times 10^{-9}$	$1.053\,65 \times 10^{-9}$	4.8×10^{-4}
100.0	$-6.463\,05 \times 10^{-10}$ [6×10^{-5}] [4×10^{-5}]	$6.238\,06 \times 10^{-10}$	$6.236\,28 \times 10^{-10}$	2.9×10^{-4}
120.0	$-2.590\,96 \times 10^{-10}$ [5×10^{-5}] [3×10^{-5}]	$2.515\,73 \times 10^{-10}$	$2.514\,96 \times 10^{-10}$	3.1×10^{-4}
150.0	$-8.471\,72 \times 10^{-11}$ [4×10^{-5}] [6×10^{-5}]	$8.274\,75 \times 10^{-11}$	$8.272\,79 \times 10^{-11}$	2.4×10^{-4}

respectively (recall the two one-sided values are expected to agree with each other, within numerical error). In each table we indicate separately the two contributions $[F^r_{l\le 15}]_\pm$ and $[F^r_{l>15}]_\pm$, where the former is the part calculated directly using our evolution code, and the latter is the extrapolated contribution from $l > 15$, calculated as explained in Sec. III E above. The large-l tail contributes at most 2% of the total SF (depending on r_0). The relative fractional error in $[F^r_{l>15}]_\pm$ [i.e., $\Delta_{\rm tail,rel}$, calculated through Eq. (48)] is at most comparable to (and mostly much smaller than) the fractional discretization error in $[F^r_{l\le 15}]_\pm$, which itself is at most $\sim 10^{-3}$.

In Table IV we present our final results for the radial component: the SF as a function of the orbital radius r_0. As the "final" result we quote the *average* between the two (nearly identical) one-sided values. The third column displays the magnitude of the *difference* between the two one-sided values, which is entirely due to computational error. The relative magnitude of this error (given in square brackets in the third column) is in all cases much smaller than the fractional discretization error in F^r. The latter error, given in square brackets in the second column, is taken as the average between the two one-sided discretization errors $\Delta^r_{\rm discr}$ estimated from Eq. (42).

The last column of Table IV displays the estimated error from residual nonstationarity of the numerical solutions (from residual spurious initial waves). Displayed is the difference in the values F^r obtained at different evolution times (as explained in more detail in Sec. IV B above). The values in square brackets in the last column show the fractional error from nonstationarity relative to the total SF. This error is in all cases much smaller than the discretization error.

Thus, the dominant source of error in our analysis is associated with the finite-grid discretization of the field equations. We estimate our final results for F^r to be correct to within at least $\sim 0.1\%$ for all orbital radii considered. The results for $10M \lesssim r_0 \lesssim 20M$ are likely to be correct to within $\sim 0.01\%$, and the results for $r_0 \gtrsim 20M$ to within mere $\sim 0.001\%$.

We plot $F^r(r_0)$ in Fig. 8. The radial SF is "repulsive" (i.e., acting outward, away from the central black hole) for all r_0. At large orbital radii the numerical data can be fitted analytically as

$$F^r(r_0 \gg M) \simeq \frac{\mu^2}{r_0^2}\left[a_0 + a_1\frac{M}{r_0} + a_2\left(\frac{M}{r_0}\right)^2 + a_3\left(\frac{M}{r_0}\right)^3\right], \quad (56)$$

with

$$a_0 = 1.999\,991, \qquad a_1 = -6.9969,$$
$$a_2 = 6.29, \qquad a_3 = -24.6. \quad (57)$$

This formula reproduces the numerical data within the numerical accuracy [$\lesssim 10^{-3}$] for all $r_0 \ge 8M$. The leading-order term, $F^r \simeq a_0\mu^2/r_0^2 \simeq 2\mu^2/r_0^2$ is consistent

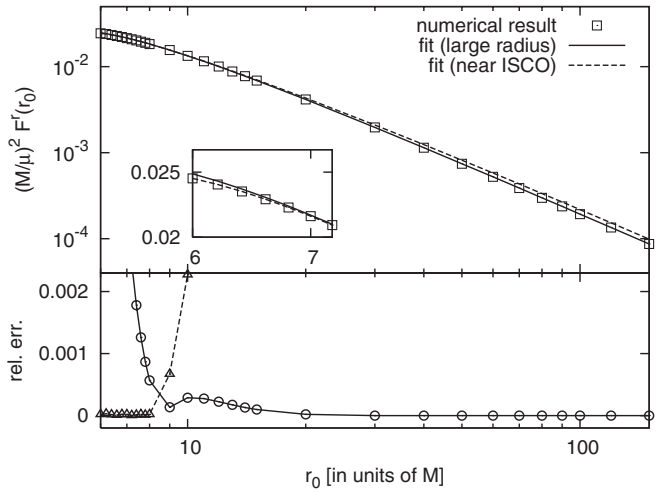

FIG. 8. The radial component of the SF. The data in the upper panel correspond to the second column in Table IV. The inset shows an expansion of the ISCO area. The solid line is a plot of the large-r_0 analytic fit given in Eq. (56). The dashed line represents the complementary near-ISCO fit (58). The lower panel shows the relative difference between the numerical data and values obtained using the analytic-fit formulas. Using the large-r_0 fit for $r_0 \ge 8M$ and the near-ISCO fit for $6M \le r_0 \le 8M$, one recovers all numerical data to within the numerical accuracy.

with the "Keplerian" SF describing the backreaction effect from the motion of the black hole about the system's center of mass (we discuss this below, when considering the SF correction to the orbital frequency). Near the innermost stable circular orbit (ISCO), $r_0 = 6M$, we fit the numerical data analytically as

$$F^r(r_0 \gtrsim 6M) \simeq \frac{\mu^2}{r_0^2}(1 - 2M/r_0)(b_0 + b_1 x_0 + b_2 x_0^2 + b_3 x_0^3), \quad (58)$$

where $x_0 \equiv 1 - 6M/r_0$ and the "best-fit" parameters (based on data in $6M \le r_0 \le 8M$) are given by

$$b_0 = 1.321\,20, \qquad b_1 = 1.2391,$$
$$b_2 = -1.297, \qquad b_3 = 1.07. \quad (59)$$

This reproduces the numerical data within the numerical accuracy for all $r_0 \le 8M$ [46].

C. Conservative shift in the orbital parameters

Given F^r, we can calculate the shift in the orbital energy and angular momentum parameters using Eq. (8). The relative shifts $\Delta\mathcal{E} \equiv (\mathcal{E} - \mathcal{E}_0)/\mathcal{E}_0$ and $\Delta\mathcal{L} \equiv (\mathcal{L} - \mathcal{L}_0)/\mathcal{L}_0$ are plotted in Fig. 9. Recall that this effect is gauge dependent; the values computed here for $\Delta\mathcal{E}$ and $\Delta\mathcal{L}$ are the Lorenz-gauge values.

The shift in the orbital frequency Ω_0 can be derived from Eq. (9). At large r_0 we obtain, using Eq. (56),

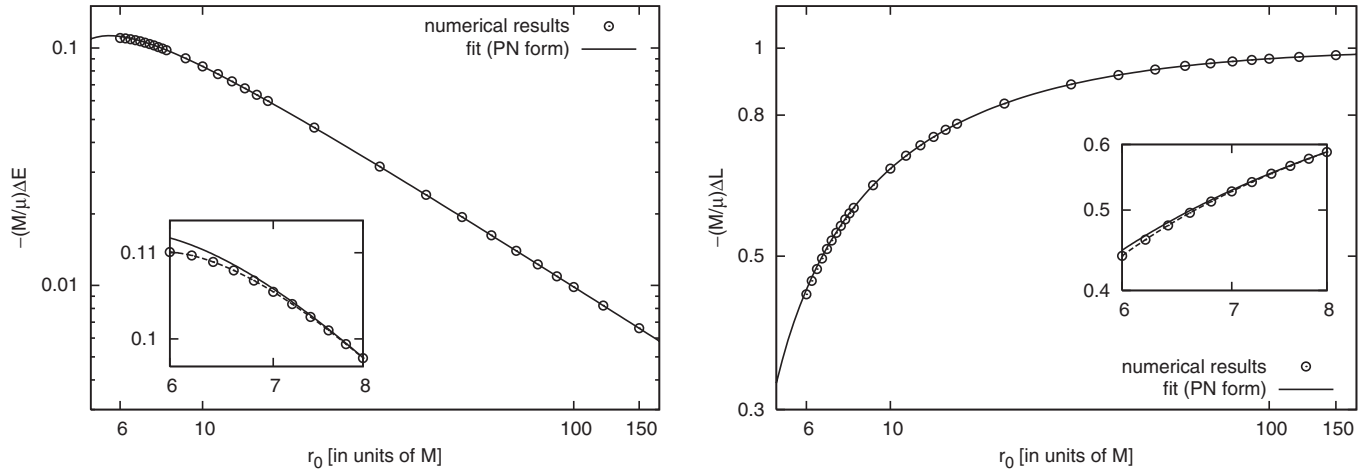

FIG. 9. The shift in the energy (left panel) and angular momentum (right panel) parameters, due to the conservative SF effect. The plots show the relative shifts $\Delta\mathcal{E} \equiv (\mathcal{E} - \mathcal{E}_0)/\mathcal{E}_0$ and $\Delta\mathcal{L} \equiv (\mathcal{L} - \mathcal{L}_0)/\mathcal{L}_0$, where $\mathcal{E}_0$ and $\mathcal{L}_0$ are the geodesic values. Solid and dashed lines correspond to the large-r_0 and near-ISCO analytic fits, Eqs. (56) and (58), respectively. Recall $\Delta\mathcal{E}$ and $\Delta\mathcal{L}$ are gauge dependent; the values shown here are the Lorenz-gauge values.

$$\Omega^2(r_0 \gg M) \simeq \Omega_0^2\left\{1 + \frac{\mu}{M}\left[-a_0 + c_1\frac{M}{r_0} + c_2\left(\frac{M}{r_0}\right)^2 + c_3\left(\frac{M}{r_0}\right)^3\right]\right\}, \tag{60}$$

where $c_1 = 3a_0 - a_1$, $c_2 = 3a_1 - a_2$, and $c_3 = 3a_2 - a_3$, with the coefficients a_n given in Eq. (57). The term proportional to $a_0(\simeq 2)$ is precisely the "Newtonian" SF [see, e.g., Eq. (2) of [36]], which dominates the SF effect at $r_0 \gg M$. This piece of the force is simply the $O(\mu)$ difference between the standard Keplerian frequency $\Omega^2 = (M + \mu)/R^3$ (expressed in terms of the separation R) and $\Omega_0^2 = M/r_0^3$, with the separation R related to the "center-of-mass" distance r_0 through $M(R - r_0) = \mu r_0$. The rest of the terms in Eq. (60) are general relativistic (3PN) corrections. We define $\Delta(\Omega^2)_{\rm GR} \equiv (\Omega^2 - \Omega_0^2)/\Omega_0^2 + 2\mu/M$, and in Fig. 10 plot $\Delta(\Omega^2)_{\rm GR}$ as a function of r_0.

It is natural to ask how our result for Ω compares, at large r_0, with results from PN literature. We must first note that, although Ω_0 is gauge invariant, r_0 itself is not, and so the functional form of $\Omega(r_0)$ in Eq. (60) is gauge dependent. This makes it difficult to compare with the standard (nonperturbative) PN result [47], which is given in a particular coordinate gauge (the "harmonic" gauge) that, in a perturbative context, does not coincide with the Lorenz gauge employed here. Another calculation of the conservative PN SF was carried out recently by Nakano [48], within perturbation theory, using a modified version of the Regge-Wheelar gauge. The results from this calculation, too, cannot be directly compared to ours, because of the different gauges used.

One may attempt to circumvent the gauge ambiguity problem by writing down an expression (in a PN form) for one gauge-invariant quantity in terms of a second gauge-invariant quantity—such an expression would be "truly" gauge invariant and would allow direct comparison between calculations done in different gauges. For circular orbits, both Ω and $S \equiv \mathcal{E} - \Omega\mathcal{L}$ are gauge invariant (see Sec. II B), and we may attempt an expression of the form $S(\Omega)$. Introducing the new gauge-invariant variable $x \equiv (M\Omega)^{1/3}$, we obtain, at 3PN,

$$S = 1 - \tfrac{3}{2}x^2 - \tfrac{9}{8}x^4 - \tfrac{27}{16}x^6 + O(\mu^2), \tag{61}$$

with a vanishing $O(\mu)$ term. Hence, $S(x)$ is not useful for comparing the conservative SF effect in the case of a circular orbit. Comparison of our results with results from PN literature is not at all straightforward, and we leave it for future work.

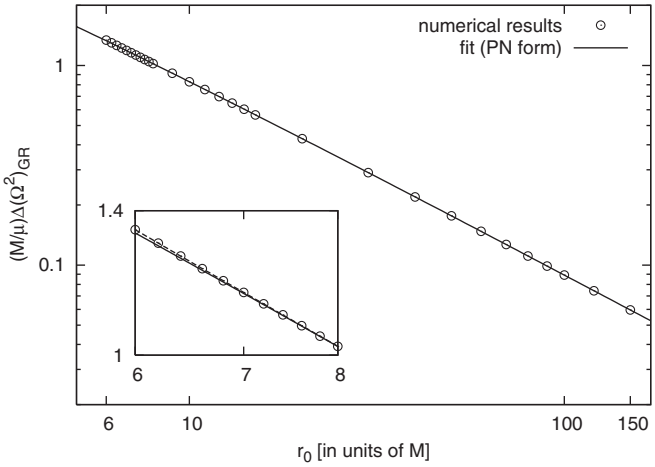

FIG. 10. Shift in the orbital frequency due to the conservative SF effect. Shown is the quantity $\Delta(\Omega^2)_{\rm GR} \equiv (\Omega^2 - \Omega_0^2)/\Omega_0^2 - (-2\mu/M)$, describing the relative shift in Ω^2, minus the leading-order Keplerian term. The solid line shows the large-r_0 (3PN) analytic fit, Eq. (60). The dashed line corresponds to the near-ISCO fit (58).

VI. CONCLUDING REMARKS AND FUTURE APPLICATIONS

This work marks a minor milestone in a long-term program aimed to develop the theoretical and practical tools for computing EMRI orbits (and, eventually, their gravitational waveforms). We compute here for the first time the gravitational SF in an example of a particle orbiting a black hole, demonstrating the applicability of our approach, whose main elements are (i) direct solution for the metric perturbation, in the Lorenz gauge; (ii) numerical evolution in the time domain; and (iii) use of the mode-sum scheme to derive the local SF. In the case of a strictly circular orbit, the analysis of the local SF provides us with little new physics: The radiative effect is well known from energy-balance analysis, and the conservative force does not have a strict gauge-invariant significance. Calculation of gauge-invariant conservative effects (like the shift in the ISCO frequency, or the correction to the rate of perihelion precession) requires analysis of (at least slightly) noncircular orbits. In follow-up work we intend to extend our analysis to eccentric orbits (see below), which would gain us access to this more interesting physics.

Self-force calculations bring about major issues of computational cost and computational efficiency. All computations in this work were carried out on a standard desktop computer (3 GHz dual-processor, with 4 Gb of RAM). Calculation of the SF at a single strong-field point, with fractional accuracy $\lesssim 10^{-3}$, took $\sim$2 hours of CPU time. This is practical enough for studying the simple one-parameter family of circular orbits, but may not be practical for studying more general orbits. There are a few obvious ways by which one may improve the efficiency of the numerical algorithm: (1) Our evolution code currently utilizes a uniform grid. This is very inefficient, since the resolution requirement near the worldline is much higher than anywhere else on the 2-dimensional grid. Our problem naturally calls for a mesh-refinement treatment. This is a standard technique in numerical relativity, but its application would require a major modification of our code. (2) We may try to improve the rate of decay of the initial spurious waves, by using the stationary numerical solutions obtained with low resolution as initial conditions for the evolution at higher resolution. This will allow to evolve for shorter periods, hence saving computation time. It should be straightforward to implement such a procedure. (3) In the present analysis we conservatively set the same accuracy threshold for each individual l mode of the force. Since the contribution of the individual modes to the total SF vary over a few orders of magnitude, this procedure is not very economic. It would be better to use an algorithm which incorporates a threshold on the total force. This, too, could be implemented rather easily.

Since our code is based on time-domain evolution (with no frequency decomposition), it is readily extensible to deal with any orbit in Schwarzschild spacetime. The finite-difference algorithm would change slightly (it would resemble the algorithm used for radial plunge trajectories [13,20]), but the stability features and resolution requirements of the code would not change. Work to extend our analysis to eccentric orbits is now in progress.

It is more challenging to apply our approach for orbits in Kerr spacetime. In this case we may no longer rely on a spherical-harmonic decomposition of the field equations, and—insisting on a time-domain analysis in the Lorenz gauge—we would have to apply time evolution in 2 + 1D. The challenge here is two-fold: First, the solutions to the 2 + 1D field equations are no longer continuous along the worldline (as in the 1 + 1D case), but rather diverge there logarithmically. Second, a stable numerical scheme for evolution of Lorenz-gauge perturbations in 2 + 1D is yet to be developed. A numerical scheme for dealing with the first of the above difficulties had been outlined in Sec. V of BL, and was recently implemented for a scalar-field toy model [49].

ACKNOWLEDGMENTS

This work was supported by PPARC through Grant No. PP/D001110/1. L. B. also gratefully acknowledges financial support from the Nuffield Foundation. N. S. thanks Hiroyuki Nakano and Misao Sasaki for helpful discussions.

APPENDIX A: FIELD EQUATIONS AND GAUGE CONDITIONS FOR THE PERTURBATION FUNCTIONS $\bar{h}^{(i)lm}(r,t)$

We give here explicit expressions for the various terms appearing in our basic set of mode-decomposed field equations (19). We use the notation $f = 1 - 2M/r$, $f' = 2M/r^2$, $f_0 = 1 - 2M/r_0$, and $\lambda = (l+2)(l-1)$. ∂_r is taken with fixed t, and ∂_v is taken with fixed u (v and u are the standard Eddington-Finkelstein coordinates). For brevity we occasionally omit the indices l, m.

The terms $\mathcal{M}^{(i)}_{(j)}\bar{h}^{(j)}$ in Eqs. (19) are given by

$$\mathcal{M}^{(1)}_{(j)}\bar{h}^{(j)} = \frac{1}{2}f^2 f'\bar{h}^{(3)}_{,r} + \frac{f}{2r^2}(1-4M/r)(\bar{h}^{(1)} - \bar{h}^{(5)} - f\bar{h}^{(3)}) - \frac{f^2}{2r^2}(1-6M/r)\bar{h}^{(6)}, \tag{A1}$$

$$\mathcal{M}^{(2)}_{(j)}\bar{h}^{(j)} = \frac{1}{2}f^2 f'\bar{h}^{(3)}_{,r} + f'(\bar{h}^{(2)}_{,v} - \bar{h}^{(1)}_{,v}) + \frac{f^2}{2r^2}(\bar{h}^{(2)} - \bar{h}^{(4)}) - \frac{ff'}{2r}(\bar{h}^{(1)} - \bar{h}^{(5)} - f\bar{h}^{(3)} - 2f\bar{h}^{(6)}), \tag{A2}$$

$$\mathcal{M}^{(3)}_{(j)}\bar{h}^{(j)} = -\frac{f}{2r^2}[\bar{h}^{(1)} - \bar{h}^{(5)} - (1-4M/r)(\bar{h}^{(3)} + \bar{h}^{(6)})], \tag{A3}$$

$$\mathcal{M}^{(4)}_{(j)}\bar{h}^{(j)} = \frac{1}{2}f'(\bar{h}^{(4)}_{,v} - \bar{h}^{(5)}_{,v}) - \frac{1}{2}l(l+1)(f/r^2)\bar{h}^{(2)} - \frac{1}{4}f'f/r[3\bar{h}^{(4)} + 2\bar{h}^{(5)} - \bar{h}^{(7)} + l(l+1)\bar{h}^{(6)}], \tag{A4}$$

$$\mathcal{M}^{(5)}_{(j)}\bar{h}^{(j)} = \frac{f}{r^2}\Big[(1-4.5M/r)\bar{h}^{(5)} - \frac{1}{2}l(l+1)(\bar{h}^{(1)} - f\bar{h}^{(3)}) + \frac{1}{2}(1-3M/r)(l(l+1)\bar{h}^{(6)} - \bar{h}^{(7)})\Big], \tag{A5}$$

$$\mathcal{M}^{(6)}_{(j)}\bar{h}^{(j)} = -\frac{f}{2r^2}[\bar{h}^{(1)} - \bar{h}^{(5)} - (1-4M/r)(\bar{h}^{(3)} + \bar{h}^{(6)})], \tag{A6}$$

$$\mathcal{M}^{(7)}_{(j)}\bar{h}^{(j)} = -\frac{f}{2r^2}(\bar{h}^{(7)} + \lambda\bar{h}^{(5)}), \tag{A7}$$

$$\mathcal{M}^{(8)}_{(j)}\bar{h}^{(j)} = \frac{1}{2}f'(\bar{h}^{(8)}_{,v} - \bar{h}^{(9)}_{,v}) - \frac{1}{4}f'f/r(3\bar{h}^{(8)} + 2\bar{h}^{(9)} - \bar{h}^{(10)}), \tag{A8}$$

$$\mathcal{M}^{(9)}_{(j)}\bar{h}^{(j)} = \frac{f}{r^2}(1-4.5M/r)\bar{h}^{(9)} - \frac{f}{2r^2}(1-3M/r)\bar{h}^{(10)}, \tag{A9}$$

$$\mathcal{M}^{(10)}_{(j)}\bar{h}^{(j)} = -\frac{f}{2r^2}(\bar{h}^{(10)} + \lambda\bar{h}^{(9)}). \tag{A10}$$

For a circular equatorial geodesic orbit with $r = r_0$ [hence with t-frequency $\Omega_0 = (M/r_0^3)^{1/2}$ and specific energy $\mathcal{E}_0 = (1-2M/r_0)(1-3M/r_0)^{-1/2}$], the source terms $S^{(i)lm}$ in Eqs. (19) read

$$S^{(i)lm}(r,t) = 4\pi\mathcal{E}_0\alpha^{(i)}\delta(r-r_0)\times\begin{cases} Y^{lm*}(\pi/2,\Omega_0 t), & i=1\text{–}7 \quad \text{(even parity modes)},\\ Y^{lm*}_{,\theta}(\pi/2,\Omega_0 t), & i=8\text{–}10 \quad \text{(odd parity modes)}.\end{cases} \tag{A11}$$

The coefficients $\alpha^{(i)}$ are given by

$$\begin{aligned} &\alpha^{(1)} = f_0^2/r_0, \qquad \alpha^{(3)} = f_0/r_0,\\ &\alpha^{(2)} = \alpha^{(5)} = \alpha^{(9)} = 0, \qquad \alpha^{(4)} = 2if_0 m\Omega_0,\\ &\alpha^{(6)} = r_0\Omega_0^2, \qquad \alpha^{(7)} = r_0\Omega_0^2[l(l+1) - 2m^2],\\ &\alpha^{(8)} = 2f_0\Omega_0, \qquad \alpha^{(10)} = 2imr_0\Omega_0^2. \end{aligned} \tag{A12}$$

The four Lorenz-gauge conditions $\bar{h}_{\alpha\beta}{}^{;\beta} = 0$ translate, upon decomposing in tensor harmonics, to four constraints on the time-radial functions $\bar{h}^{(i)}$. These read

$$-\bar{h}^{(1)}_{,t} + f(-\bar{h}^{(3)}_{,t} + \bar{h}^{(2)}_{,r} + \bar{h}^{(2)}/r - \bar{h}^{(4)}/r) = 0, \tag{A13}$$

$$\bar{h}^{(2)}_{,t} - f\bar{h}^{(1)}_{,r} + f^2\bar{h}^{(3)}_{,r} - (f/r)(\bar{h}^{(1)} - \bar{h}^{(5)} - f\bar{h}^{(3)} - 2f\bar{h}^{(6)}) = 0, \tag{A14}$$

$$\bar{h}^{(4)}_{,t} - f(\bar{h}^{(5)}_{,r} + 2\bar{h}^{(5)}/r + l(l+1)\bar{h}^{(6)}/r - \bar{h}^{(7)}/r) = 0, \tag{A15}$$

$$\bar{h}^{(8)}_{,t} - f(\bar{h}^{(9)}_{,r} + 2\bar{h}^{(9)}/r - \bar{h}^{(10)}/r) = 0. \tag{A16}$$

APPENDIX B: FORMULAS FOR THE COEFFICIENTS $f^r_{n\pm}$ AND $f^t_{n\pm}$

We give here formulas for constructing the various coefficients $f^{\alpha}_{n\pm}$ appearing in Eq. (29), using the Lorenz-gauge metric perturbation fields $\bar{h}^{(i)lm}(r,t)$ and their derivatives. For brevity we omit the superscripts l, m from both the $f^{\alpha lm}_{n\pm}$'s and the $\bar{h}^{(i)lm}$'s. We use here the notation $\tilde{\mathcal{L}}_0 = \mathcal{L}_0/r_0$, where, recall, $\mathcal{L}_0$ is given in Eq. (4). Also recall $\mathcal{E}_0$ is given in Eq. (3), $f_0 = (1-2M/r_0)$, and $\lambda = (l+2)(l-1)$. r derivatives are taken with fixed t, and t derivatives are taken with fixed r. All functions $\bar{h}^{(i)lm}$ and their derivatives in the expressions below are evaluated at $r = r_0$ and $t = t_0$. Subscripts "$\pm$" refer to taking r derivatives from $r \to r_0^{\pm}$ (we omit these subscripts whenever $f^{\alpha}_{n+} = f^{\alpha}_{n-}$).

For the r component we have

$$f^r_{0\pm} = \mathcal{E}_0^2(M/r_0)f_0^{-2}\bar{h}^{(1)} + \frac{1}{4}\mathcal{E}_0^2 f_0^{-2}(r_0 f_0\bar{h}^{(1)}_{,r} - \bar{h}^{(1)}) + \frac{1}{4}\tilde{\mathcal{L}}_0^2 f_0(r_0\bar{h}^{(3)}_{,r} - \bar{h}^{(3)}) + \frac{1}{4}f_0(r_0\bar{h}^{(6)}_{,r} - \bar{h}^{(6)}) + \frac{im\mathcal{E}_0\tilde{\mathcal{L}}_0 r_0}{2l(l+1)}\bar{h}^{(4)}_{,r} - \frac{m^2\tilde{\mathcal{L}}_0^2 f_0}{4l(l+1)\lambda}(r_0\bar{h}^{(7)}_{,r} + \bar{h}^{(7)}), \tag{B1}$$

$$f^r_{1\pm} = \frac{1}{4}\tilde{\mathcal{L}}_0^2(-2\bar{h}^{(1)} + 2f_0\bar{h}^{(3)} + f_0\bar{h}^{(6)} + r_0 f_0\bar{h}^{(6)}_{,r}), \tag{B2}$$

$$f^r_{2\pm} = \frac{\tilde{\mathcal{L}}_0^2}{4l(l+1)}[-2\bar{h}^{(5)} + (f_0/\lambda)(r_0\bar{h}^{(7)}_{,r} + \bar{h}^{(7)})], \tag{B3}$$

$$f^r_{3\pm} = -\frac{\tilde{\mathcal{L}}_0^2 f_0}{4l(l+1)\lambda}(r_0\bar{h}^{(7)}_{,r} + \bar{h}^{(7)}), \tag{B4}$$

$$f^r_{4\pm} = \frac{im\tilde{\mathcal{L}}_0^2}{2l(l+1)}[-\bar{h}^{(9)} + (f_0/\lambda)(r_0\bar{h}^{(10)}_{,r} + \bar{h}^{(10)})], \tag{B5}$$

$$f^r_{5\pm} = \frac{\tilde{\mathcal{L}}_0\mathcal{E}_0 r_0}{2f_0 l(l+1)}(\bar{h}^{(9)}_{,t} - f_0\bar{h}^{(8)}_{,r}), \tag{B6}$$

$$f^r_6 = f^r_7 = 0. \tag{B7}$$

For the t component we have

$$f^t_0 = -\frac{1}{4}\mathcal{E}_0^2\tilde{\mathcal{L}}_0^2 f_0^{-3} r_0 \bar{h}^{(1)}_{,t} + \frac{1}{4} im\mathcal{E}_0\tilde{\mathcal{L}}_0(2f_0 - \mathcal{E}_0^2) f_0^{-3}\bar{h}^{(1)} + \frac{1}{2}\mathcal{E}_0^2\tilde{\mathcal{L}}_0^2 f_0^{-3}(M/r_0)\bar{h}^{(2)} - \frac{1}{4} f_0^{-2} r_0 \tilde{\mathcal{L}}_0^2(\mathcal{E}_0^2 + f_0)\bar{h}^{(3)}_{,t}$$
$$- \frac{1}{4} im\tilde{\mathcal{L}}_0^3\mathcal{E}_0 f_0^{-1}\bar{h}^{(3)} - \frac{im\mathcal{E}_0^3\tilde{\mathcal{L}}_0 f_0^{-3} r_0}{2l(l+1)}\bar{h}^{(4)}_{,t} + \frac{m^2\tilde{\mathcal{L}}_0^4 f_0^{-1}}{2l(l+1)}\bar{h}^{(4)} + \frac{im\tilde{\mathcal{L}}_0\mathcal{E}_0^3 f_0^{-3}(M/r_0)}{2l(l+1)}\bar{h}^{(5)} + \frac{1}{4}\tilde{\mathcal{L}}_0^2 f_0^{-1} r_0 \bar{h}^{(6)}_{,t}$$
$$+ \frac{1}{4} im\mathcal{E}_0\tilde{\mathcal{L}} f_0^{-1}\bar{h}^{(6)} + \frac{m^2\tilde{\mathcal{L}}_0^2(\mathcal{E}_0^2 + f_0) f_0^{-2} r_0}{4l(l+1)\lambda}\bar{h}^{(7)}_{,t} + \frac{im\mathcal{E}_0\tilde{\mathcal{L}}_0^3(m^2+4) f_0^{-1}}{4l(l+1)\lambda}\bar{h}^{(7)}, \tag{B8}$$

$$f^t_1 = -\frac{1}{2}\tilde{\mathcal{L}}_0^4 f_0^{-1}\bar{h}^{(2)} - \frac{im\mathcal{E}_0\tilde{\mathcal{L}}_0^3 f_0^{-1}}{2l(l+1)}\bar{h}^{(5)}$$
$$- \frac{1}{4}\tilde{\mathcal{L}}_0^2(\tilde{\mathcal{E}}_0^2 + f_0) f_0^{-2} r_0 \bar{h}^{(6)}_{,t} - \frac{1}{4} im\mathcal{E}_0\tilde{\mathcal{L}}_0^3 f_0^{-1}\bar{h}^{(6)}$$
$$- \frac{im\mathcal{E}_0\tilde{\mathcal{L}}_0^3 f_0^{-1}}{l(l+1)\lambda}\bar{h}^{(7)}, \tag{B9}$$

$$f^t_2 = -\frac{\tilde{\mathcal{L}}_0^4 f_0^{-1}}{2l(l+1)}\bar{h}^{(4)} - \frac{\tilde{\mathcal{L}}_0^2(\mathcal{E}_0^2 + f_0) f_0^{-2} r_0}{4l(l+1)\lambda}\bar{h}^{(7)}_{,t}$$
$$- \frac{5im\mathcal{E}_0\tilde{\mathcal{L}}_0^3 f_0^{-1}}{4l(l+1)\lambda}\bar{h}^{(7)}, \tag{B10}$$

$$f^t_3 = \frac{\tilde{\mathcal{L}}_0^2(\mathcal{E}_0^2 + f_0) r_0 f_0^{-2}}{4l(l+1)\lambda}\bar{h}^{(7)}_{,t} + \frac{im\mathcal{E}_0\tilde{\mathcal{L}}_0^3 f_0^{-1}}{4l(l+1)\lambda}\bar{h}^{(7)}, \tag{B11}$$

$$f^t_4 = -\frac{im\tilde{\mathcal{L}}_0^4 f_0^{-1}}{2l(l+1)}\bar{h}^{(8)} - \frac{im\tilde{\mathcal{L}}_0^2(\mathcal{E}_0^2 + f_0) f_0^{-2} r_0}{2l(l+1)\lambda}\bar{h}^{(10)}_{,t}$$
$$+ \frac{m^2\tilde{\mathcal{L}}_0^3\mathcal{E}_0 f_0^{-1}}{l(l+1)\lambda}\bar{h}^{(10)} \tag{B12}$$

$$f^t_5 = \frac{\mathcal{E}_0^3\tilde{\mathcal{L}}_0 f_0^{-3} r_0}{2l(l+1)}\bar{h}^{(8)}_{,t} - \frac{\mathcal{E}_0^3\tilde{\mathcal{L}}_0(M/r_0) f_0^{-3}}{2l(l+1)}\bar{h}^{(9)}$$
$$+ \frac{(m^2-1)\mathcal{E}_0\tilde{\mathcal{L}}_0^3 f_0^{-1}}{2l(l+1)\lambda}\bar{h}^{(10)}, \tag{B13}$$

$$f^t_6 = \frac{\mathcal{E}_0\tilde{\mathcal{L}}_0^3 f_0^{-1}}{2l(l+1)}(\bar{h}^{(9)} + \lambda^{-1}\bar{h}^{(10)}), \tag{B14}$$

$$f^t_7 = \frac{\mathcal{E}_0\tilde{\mathcal{L}}^3 f_0^{-1}}{2l(l+1)\lambda}\bar{h}^{(10)}. \tag{B15}$$

APPENDIX C: FORMULAS FOR THE COUPLING COEFFICIENTS

We give here formulas for reexpanding all angular functions in Eq. (29) in spherical harmonics $Y^{lm}(\theta,\varphi)$. The following identities hold for all l, m and any θ, φ. We have

$$\begin{aligned}
\sin^2\theta Y^{lm} &= \alpha^{lm}_{(+2)} Y^{l+2,m} + \alpha^{lm}_{(0)} Y^{lm} + \alpha^{lm}_{(-2)} Y^{l-2,m},\\
\cos\theta\sin\theta Y^{lm}_{,\theta} &= \beta^{lm}_{(+2)} Y^{l+2,m} + \beta^{lm}_{(0)} Y^{lm} + \beta^{lm}_{(-2)} Y^{l-2,m},\\
\sin^2\theta Y^{lm}_{,\theta\theta} &= \gamma^{lm}_{(+2)} Y^{l+2,m} + \gamma^{lm}_{(0)} Y^{lm} + \gamma^{lm}_{(-2)} Y^{l-2,m},\\
\sin\theta Y^{lm}_{,\theta} &= \delta^{lm}_{(+1)} Y^{l+1,m} + \delta^{lm}_{(-1)} Y^{l-1,m},\\
\cos\theta Y^{lm} - \sin\theta Y^{lm}_{,\theta} &= \epsilon^{lm}_{(+1)} Y^{l+1,m} + \epsilon^{lm}_{(-1)} Y^{l-1,m},\\
\sin^3\theta Y^{lm}_{,\theta} &= \zeta^{lm}_{(+3)} Y^{l+3,m} + \zeta^{lm}_{(+1)} Y^{l+1,m} + \zeta^{lm}_{(-1)} Y^{l-1,m} + \zeta^{lm}_{(-3)} Y^{l-3,m},\\
\cos\theta\sin^2\theta Y^{lm}_{,\theta\theta} &= \xi^{lm}_{(+3)} Y^{l+3,m} + \xi^{lm}_{+} Y^{l+1,m} + \xi^{lm}_{(-1)} Y^{l-1,m} + \xi^{lm}_{(-3)} Y^{l-3,m}.
\end{aligned} \tag{C1}$$

The coefficients are all constructed from

$$C_{lm} = \left[\frac{l^2 - m^2}{(2l+1)(2l-1)}\right]^{1/2}, \tag{C2}$$

using

$$\alpha^{lm}_{(+2)} = -C_{l+1,m}C_{l+2,m}, \qquad \alpha^{lm}_{(0)} = 1 - C^2_{lm} - C^2_{l+1,m},$$
$$\alpha^{lm}_{(-2)} = -C_{lm}C_{l-1,m}, \tag{C3}$$

$$\beta^{lm}_{(+2)} = lC_{l+1,m}C_{l+2,m}, \qquad \beta^{lm}_{(0)} = lC^2_{l+1,m} - (l+1)C^2_{lm},$$
$$\beta^{lm}_{(-2)} = -(l+1)C_{lm}C_{l-1,m}, \tag{C4}$$

$$\gamma^{lm}_{(+2)} = l^2 C_{l+1,m} C_{l+2,m},$$
$$\gamma^{lm}_{(0)} = m^2 - l(l+1) + l^2 C^2_{l+1,m} + (l+1)^2 C^2_{lm}, \quad \text{(C5)}$$
$$\gamma^{lm}_{(-2)} = (l+1)^2 C_{lm} C_{l-1,m},$$

$$\delta^{lm}_{(+1)} = l C_{l+1,m}, \qquad \delta^{lm}_{(-1)} = -(l+1) C_{lm}, \quad \text{(C6)}$$

$$\epsilon^{lm}_{(+1)} = (1-l) C_{l+1,m}, \qquad \epsilon^{lm}_{(-1)} = (l+2) C_{lm}, \quad \text{(C7)}$$

$$\zeta^{lm}_{(+3)} = -l C_{l+1,m} C_{l+2,m} C_{l+3,m},$$
$$\zeta^{lm}_{(+1)} = C_{l+1,m}[l(1 - C^2_{l+1,m} - C^2_{l+2,m}) + (l+1) C^2_{l,m}],$$
$$\zeta^{lm}_{(-1)} = -C_{l,m}[(l+1)(1 - C^2_{l-1,m} - C^2_{l,m}) + l C^2_{l+1,m}],$$
$$\zeta^{lm}_{(-3)} = (l+1) C_{l,m} C_{l-1,m} C_{l-2,m}, \quad \text{(C8)}$$

$$\xi^{lm}_{(+3)} = l^2 C_{l+1,m} C_{l+2,m} C_{l+3,m},$$
$$\xi^{lm}_{(+1)} = C_{l+1,m}[m^2 - l(l+1) + l^2 C^2_{l+1,m} + (l+1)^2 C^2_{l,m} + l^2 C^2_{l+2,m}],$$
$$\xi^{lm}_{(-1)} = C_{l,m}[m^2 - l(l+1) + l^2 C^2_{l+1,m} + (l+1)^2 C^2_{l,m} + (l+1)^2 C^2_{l-1,m}],$$
$$\xi^{lm}_{(-3)} = (l+1)^2 C_{l,m} C_{l-1,m} C_{l-2,m}. \quad \text{(C9)}$$

APPENDIX D: DETAILS OF NUMERICAL RESULTS FOR F^r

In this appendix we tabulate data obtained for the radial component F^r, braking it up into low-l and high-l (extrapolated) contributions, and displaying separately internal and external values. These data are used in Sec. V for error analysis.

TABLE VI. Results for the radial component of the SF, broken up into the contribution from $l \leq 15$ (computed directly using our numerical evolution code), and the contribution from the $l > 15$ tail (estimated as described in Sec. III E). Presented here are internal values of the SF (i.e., those obtained through taking one-sided derivatives of the perturbation from $r \to r_0^-$). The external values (which should be the same within numerical error) are given in Table VII below. The values in square brackets in the second column represent the fractional discretization error $\Delta^r_{\rm discr}$, as estimated using Eq. (42). $\Delta_{\rm tail,rel}$ is the relative fractional error in $F^r_{l>15}$ (i.e., error expressed at a fraction of the total SF), which is estimated using Eq. (48). In our analysis we made sure that the error from estimating the contribution from the large-l tail is kept smaller than the discretization error.

r_0/M	$[F^r_{l\leq 15}]_- \times (M/\mu)^2$	$[F^r_{l>15}]_- \times (M/\mu)^2$	$\lvert F^r_{l>15}/F^r_{l\leq 15}\rvert$	$\Delta_{\rm tail,rel}$
6.0	$2.497\,07 \times 10^{-2}$ $[5 \times 10^{-4}]$	$-5.046\,14 \times 10^{-4}$	2.0×10^{-2}	7×10^{-7}
6.2	$2.440\,97 \times 10^{-2}$ $[5 \times 10^{-4}]$	$-4.445\,91 \times 10^{-4}$	1.8×10^{-2}	8×10^{-7}
6.4	$2.378\,94 \times 10^{-2}$ $[4 \times 10^{-4}]$	$-3.939\,50 \times 10^{-4}$	1.7×10^{-2}	8×10^{-7}
6.6	$2.313\,39 \times 10^{-2}$ $[4 \times 10^{-4}]$	$-3.508\,80 \times 10^{-4}$	1.5×10^{-2}	9×10^{-7}
6.8	$2.246\,03 \times 10^{-2}$ $[3 \times 10^{-4}]$	$-3.139\,87 \times 10^{-4}$	1.4×10^{-2}	9×10^{-7}
7.0	$2.178\,12 \times 10^{-2}$ $[3 \times 10^{-4}]$	$-2.821\,79 \times 10^{-4}$	1.3×10^{-2}	9×10^{-7}
7.2	$2.110\,51 \times 10^{-2}$ $[2 \times 10^{-4}]$	$-2.545\,92 \times 10^{-4}$	1.2×10^{-2}	9×10^{-7}
7.4	$2.043\,85 \times 10^{-2}$ $[2 \times 10^{-4}]$	$-2.305\,39 \times 10^{-4}$	1.1×10^{-2}	8×10^{-7}
7.6	$1.978\,57 \times 10^{-2}$ $[2 \times 10^{-4}]$	$-2.094\,60 \times 10^{-4}$	1.1×10^{-2}	8×10^{-7}
7.8	$1.914\,96 \times 10^{-2}$ $[2 \times 10^{-4}]$	$-1.909\,04 \times 10^{-4}$	1.0×10^{-2}	8×10^{-7}
8.0	$1.853\,23 \times 10^{-2}$ $[2 \times 10^{-4}]$	$-1.745\,00 \times 10^{-4}$	9.4×10^{-3}	8×10^{-7}
9.0	1.57527×10^{-2} $[1 \times 10^{-4}]$	$-1.156\,33 \times 10^{-4}$	7.3×10^{-3}	6×10^{-7}
10.0	$1.347\,01 \times 10^{-2}$ $[2 \times 10^{-5}]$	$-8.063\,27 \times 10^{-5}$	6.0×10^{-3}	5×10^{-7}
11.0	$1.161\,03 \times 10^{-2}$ $[1 \times 10^{-5}]$	$-5.848\,61 \times 10^{-5}$	5.0×10^{-3}	4×10^{-7}
12.0	$1.009\,00 \times 10^{-2}$ $[9 \times 10^{-6}]$	$-4.377\,83 \times 10^{-5}$	4.3×10^{-3}	3×10^{-7}
13.0	$8.838\,52 \times 10^{-3}$ $[7 \times 10^{-6}]$	$-3.362\,46 \times 10^{-5}$	3.8×10^{-3}	2×10^{-7}
14.0	$7.799\,45 \times 10^{-3}$ $[8 \times 10^{-7}]$	$-2.638\,66 \times 10^{-5}$	3.4×10^{-3}	2×10^{-7}
15.0	$6.929\,24 \times 10^{-3}$ $[4 \times 10^{-6}]$	$-2.108\,75 \times 10^{-5}$	3.0×10^{-3}	2×10^{-7}
20.0	$4.165\,44 \times 10^{-3}$ $[1 \times 10^{-6}]$	$-8.387\,46 \times 10^{-6}$	2.0×10^{-3}	1×10^{-7}
30.0	$1.972\,16 \times 10^{-3}$ $[5 \times 10^{-7}]$	$-2.346\,90 \times 10^{-6}$	1.2×10^{-3}	4×10^{-8}
40.0	$1.143\,85 \times 10^{-3}$ $[2 \times 10^{-7}]$	$-9.626\,17 \times 10^{-7}$	8.4×10^{-4}	2×10^{-8}
50.0	$7.454\,33 \times 10^{-4}$ $[6 \times 10^{-8}]$	$-4.846\,66 \times 10^{-7}$	6.5×10^{-4}	2×10^{-8}
60.0	$5.238\,91 \times 10^{-4}$ $[2 \times 10^{-6}]$	$-2.773\,74 \times 10^{-7}$	5.3×10^{-4}	1×10^{-8}
70.0	$3.881\,83 \times 10^{-4}$ $[1 \times 10^{-6}]$	$-1.732\,93 \times 10^{-7}$	4.5×10^{-4}	9×10^{-9}
80.0	$2.990\,94 \times 10^{-4}$ $[9 \times 10^{-7}]$	$-1.154\,05 \times 10^{-7}$	3.9×10^{-4}	7×10^{-9}
90.0	$2.374\,87 \times 10^{-4}$ $[6 \times 10^{-7}]$	$-8.068\,02 \times 10^{-8}$	3.4×10^{-4}	5×10^{-9}
100.0	$1.931\,21 \times 10^{-4}$ $[5 \times 10^{-7}]$	$-5.859\,95 \times 10^{-8}$	3.0×10^{-4}	5×10^{-9}
120.0	$1.349\,02 \times 10^{-4}$ $[3 \times 10^{-7}]$	$-3.372\,48 \times 10^{-8}$	2.5×10^{-4}	4×10^{-9}
150.0	$8.684\,46 \times 10^{-5}$ $[2 \times 10^{-7}]$	$-1.717\,21 \times 10^{-8}$	2.0×10^{-4}	2×10^{-9}

TABLE VII. Same as Table VI, here for the external values of the SF.

r_0/M	$[F^r_{l\leq 15}]_+ \times (M/\mu)^2$	$[F^r_{l>15}]_+ \times (M/\mu)^2$	$\lvert F^r_{l>15}/F^r_{l\leq 15}\rvert$	$\Delta_{\text{tail,rel}}$
6.0	$2.497\,08 \times 10^{-2}$ $[1 \times 10^{-3}]$	$-5.046\,19 \times 10^{-4}$	2.0×10^{-2}	6×10^{-7}
6.2	$2.440\,97 \times 10^{-2}$ $[1 \times 10^{-3}]$	$-4.445\,94 \times 10^{-4}$	1.8×10^{-2}	7×10^{-7}
6.4	$2.378\,93 \times 10^{-2}$ $[1 \times 10^{-3}]$	$-3.939\,53 \times 10^{-4}$	1.7×10^{-2}	8×10^{-7}
6.6	$2.313\,37 \times 10^{-2}$ $[1 \times 10^{-3}]$	$-3.508\,83 \times 10^{-4}$	1.5×10^{-2}	8×10^{-7}
6.8	$2.246\,01 \times 10^{-2}$ $[1 \times 10^{-3}]$	$-3.139\,89 \times 10^{-4}$	1.4×10^{-2}	8×10^{-7}
7.0	$2.178\,09 \times 10^{-2}$ $[1 \times 10^{-3}]$	$-2.821\,81 \times 10^{-4}$	1.3×10^{-2}	8×10^{-7}
7.2	$2.110\,49 \times 10^{-2}$ $[9 \times 10^{-4}]$	$-2.545\,94 \times 10^{-4}$	1.2×10^{-2}	8×10^{-7}
7.4	$2.043\,82 \times 10^{-2}$ $[9 \times 10^{-4}]$	$-2.305\,43 \times 10^{-4}$	1.1×10^{-2}	8×10^{-7}
7.6	$1.978\,54 \times 10^{-2}$ $[8 \times 10^{-4}]$	$-2.094\,63 \times 10^{-4}$	1.1×10^{-2}	8×10^{-7}
7.8	$1.914\,93 \times 10^{-2}$ $[8 \times 10^{-4}]$	$-1.909\,07 \times 10^{-4}$	1.0×10^{-2}	8×10^{-7}
8.0	$1.853\,20 \times 10^{-2}$ $[8 \times 10^{-4}]$	$-1.745\,03 \times 10^{-4}$	9.4×10^{-3}	7×10^{-7}
9.0	$1.575\,24 \times 10^{-2}$ $[6 \times 10^{-4}]$	$-1.156\,36 \times 10^{-4}$	7.3×10^{-3}	6×10^{-7}
10.0	$1.347\,01 \times 10^{-2}$ $[1 \times 10^{-4}]$	$-8.063\,38 \times 10^{-5}$	6.0×10^{-3}	5×10^{-7}
11.0	$1.161\,03 \times 10^{-2}$ $[1 \times 10^{-4}]$	$-5.848\,73 \times 10^{-5}$	5.0×10^{-3}	4×10^{-7}
12.0	$1.009\,00 \times 10^{-2}$ $[9 \times 10^{-5}]$	$-4.377\,89 \times 10^{-5}$	4.3×10^{-3}	3×10^{-7}
13.0	$8.838\,52 \times 10^{-3}$ $[7 \times 10^{-5}]$	$-3.362\,81 \times 10^{-5}$	3.8×10^{-3}	1×10^{-7}
14.0	$7.799\,46 \times 10^{-3}$ $[3 \times 10^{-5}]$	$-2.638\,86 \times 10^{-5}$	3.4×10^{-3}	1×10^{-7}
15.0	$6.929\,24 \times 10^{-3}$ $[5 \times 10^{-5}]$	$-2.108\,86 \times 10^{-5}$	3.0×10^{-3}	1×10^{-7}
20.0	$4.165\,44 \times 10^{-3}$ $[3 \times 10^{-5}]$	$-8.387\,36 \times 10^{-6}$	2.0×10^{-3}	2×10^{-7}
30.0	$1.972\,16 \times 10^{-3}$ $[1 \times 10^{-5}]$	$-2.346\,82 \times 10^{-6}$	1.2×10^{-3}	5×10^{-8}
40.0	$1.143\,85 \times 10^{-3}$ $[4 \times 10^{-6}]$	$-9.626\,03 \times 10^{-7}$	8.4×10^{-4}	2×10^{-8}
50.0	$7.454\,33 \times 10^{-4}$ $[2 \times 10^{-6}]$	$-4.846\,63 \times 10^{-7}$	6.5×10^{-4}	1×10^{-8}
60.0	$5.238\,91 \times 10^{-4}$ $[3 \times 10^{-5}]$	-2.77373×10^{-7}	5.3×10^{-4}	1×10^{-8}
70.0	$3.881\,83 \times 10^{-4}$ $[2 \times 10^{-5}]$	$-1.732\,93 \times 10^{-7}$	4.5×10^{-4}	9×10^{-9}
80.0	$2.990\,94 \times 10^{-4}$ $[2 \times 10^{-5}]$	$-1.154\,05 \times 10^{-7}$	3.9×10^{-4}	7×10^{-9}
90.0	$2.374\,87 \times 10^{-4}$ $[1 \times 10^{-5}]$	$-8.068\,02 \times 10^{-8}$	3.4×10^{-4}	4×10^{-9}
100.0	$1.931\,21 \times 10^{-4}$ $[1 \times 10^{-5}]$	$-5.859\,92 \times 10^{-8}$	3.0×10^{-4}	5×10^{-9}
120.0	$1.349\,02 \times 10^{-4}$ $[7 \times 10^{-6}]$	$-3.372\,49 \times 10^{-8}$	2.5×10^{-4}	4×10^{-9}
150.0	$8.684\,46 \times 10^{-5}$ $[4 \times 10^{-6}]$	$-1.717\,21 \times 10^{-8}$	2.0×10^{-4}	4×10^{-9}

[1] B. S. DeWitt and R. W. Brehme, Ann. Phys. (N.Y.) **9**, 220 (1960).
[2] Y. Mino, M. Sasaki, and T. Tanaka, Phys. Rev. D **55**, 3457 (1997).
[3] T. C. Quinn and R. M. Wald, Phys. Rev. D **56**, 3381 (1997).
[4] T. C. Quinn, Phys. Rev. D **62**, 064029 (2000).
[5] S. Detweiler and B. F. Whiting, Phys. Rev. D **67**, 024025 (2003).
[6] L. Barack and A. Ori, Phys. Rev. D **61**, 061502 (2000).
[7] L. Barack, Phys. Rev. D **64**, 084021 (2001).
[8] L. Barack, Y. Mino, H. Nakano, A. Ori, and M. Sasaki, Phys. Rev. Lett. **88**, 091101 (2002).
[9] L. Barack and A. Ori, Phys. Rev. D **67**, 024029 (2003).
[10] L. Barack and A. Ori, Phys. Rev. Lett. **90**, 111101 (2003).
[11] L. M. Burko, Classical Quantum Gravity **17**, 227 (2000).
[12] L. M. Burko and Y. T. Liu, Phys. Rev. D **64**, 024006 (2001).
[13] L. Barack and L. M. Burko, Phys. Rev. D **62**, 084040 (2000).
[14] L. M. Burko, Phys. Rev. Lett. **84**, 4529 (2000).
[15] S. Detweiler, E. Messaritaki, and B. F. Whiting, Phys. Rev. D **67**, 104016 (2003).
[16] L. M. Diaz-Rivera, E. Messaritaki, B. F. Whiting, and S. Detweiler, Phys. Rev. D **70**, 124018 (2004).
[17] W. Hikida, S. Jhingan, H. Nakano, N. Sago, M. Sasaki, and T. Tanaka, Prog. Theor. Phys. **113**, 283 (2005).
[18] W. Hikida (unpublished); Talk in the eighth Capra meeting at Abingdon (2005).
[19] R. Haas (work in progress); Talk in the ninth Capra meeting at UWM (2006).
[20] L. Barack and C. O. Lousto, Phys. Rev. D **66**, 061502 (2002).
[21] T. S. Keidl, J. L. Friedman, and A. G. Wiseman, gr-qc/0611072.
[22] W. Hikida, H. Nakano, and M. Sasaki, Classical Quantum Gravity **22**, S753 (2005).
[23] E. Poisson, Living Rev. Relativity **7**, 6 (2004).
[24] C. O. Lousto, Classical Quantum Gravity **22**, 15 (2005).
[25] L. Barack and C. Cutler, Phys. Rev. D **69**, 082005 (2004).
[26] P. L. Chrzanowski, Phys. Rev. D **11**, 2042 (1975).
[27] T. Regge and J. A. Wheeler, Phys. Rev. **108**, 1063 (1957).

[28] Y. Mino, Prog. Theor. Phys. **99**, 79 (1998).
[29] Y. Mino and H. Nakano, Prog. Theor. Phys. **100**, 507 (1998).
[30] H. Nakano and M. Sasaki, Prog. Theor. Phys. **105**, 197 (2001).
[31] L. Barack and A. Ori, Phys. Rev. D **64**, 124003 (2001).
[32] By "multipole modes" we mean here, and throughout this paper, the components of a spacetime function in a spherical-harmonic basis defined on 2-spheres *centered at the black hole* (and not at the particle), as usual in black hole perturbation theory.
[33] L. Barack and C. O. Lousto, Phys. Rev. D **72**, 104026 (2005).
[34] S. Detweiler and E. Poisson, Phys. Rev. D **69**, 084019 (2004).
[35] C. W. Misner, K. S. Thorne, and J. A. Wheeler, *Gravitation* (Freeman, San Francisco, 1973).
[36] S. Detweiler, Classical Quantum Gravity **22**, S681 (2005).
[37] We use here the same notation and definitions as in BL, except for a redefinition $\bar{h}^{(3)}[\text{here}] = (1 - 2M/r)^{-1}\bar{h}^{(3)}[\text{BL}]$. This simplifies slightly the form of the perturbation equations (19), and is motivated by the fact that $\bar{h}^{(3)}[\text{BL paper}]$ vanishes at the horizon. Also, we fix here an error in Eq. (20) of BL: The factor "i" in the expressions for $h^{lm}_{r\varphi}$ and $h^{lm}_{\theta\varphi}$ is erroneous and we omit it here.
[38] A. Ori, Phys. Rev. D **70**, 124027 (2004).
[39] F. J. Zerilli, Phys. Rev. D **2**, 2141 (1970).
[40] C. O. Lousto and R. H. Price, Phys. Rev. D **56**, 6439 (1997).
[41] K. Martel and E. Poisson, Phys. Rev. D **66**, 084001 (2002).
[42] K. Martel, Phys. Rev. D **69**, 044025 (2004).
[43] W. H. Press, S. A. Teukolsky, W. T. Vetterling, and B. P. Flannery, *Numerical Recipes* (Cambridge University Press, Cambridge, England, 1992).
[44] S. A. Teukolsky, Astrophys. J. **185**, 635 (1973).
[45] S. A. Teukolsky and W. H. Press, Astrophys. J. **193**, 443 (1974).
[46] The analytic-fit formula (58) should not be regarded as representing the first few terms in a convergent expansion in $x \equiv 1 - 6M/r_0$; in fact, it is evident from Fig. 8 (lower panel) that such a series is likely to have a very small radius of convergence around $r_0 = 6M$. We give the analytic fit (58) merely for practical reasons, as it correctly gives the value of the SF anywhere in the strong-field regime $6M \leq r_0 \leq 8M$ to within our numerical error ($\lesssim 10^{-3}$).
[47] L. Blanchet, Living Rev. Relativity **9**, 4 (2006).
[48] H. Nakano (unpublished); Presentation at the ninth Capra meeting at UWM (2006).
[49] L. Barack and D. A. Golbourn (unpublished).